Comparison of Video and CCD Cameras in Online Portal Imagers Calibrated for Dosimetry

by

Cristina Dawn Spanu Tollefsen

A practicum submitted to the Faculty of Graduate Studies
in partial fulfillment of the requirements
for the degree of

Master of Science

Department of Physics
University of Manitoba

THE UNIVERSITY OF MANITOBA

FACULTY OF GRADUATE STUDIES

*****

COPYRIGHT PERMISSION PAGE

Comparison of Video and CCD Cameras in Online Portal Imagers Calibrated for Dosimetry

BY

Cristina Dawn Spanu Tollefsen

A Thesis/Practicum submitted to the Faculty of Graduate Studies of The University of Manitoba in partial fulfillment of the requirements of the degree of Master of Science

Abstract

Video-based electronic portal imaging devices (EPIDs) are the most common type of portal imager found in clinical practice. In addition to providing a method to detect and correct patient set-up errors and record treatments, possibilities exist for the dosimetric use of video-based EPIDs. To determine if a particular system is suitable for dosimetry, the entire system and especially the camera should be thoroughly tested and calibrated. Comparisons were made of the performance of a Newvicon camera and a CCD camera in a video-based EPID. Tests were performed on the cameras to investigate linearity, noise, frame grabber effects, clamping error, and lens vignetting. Tests of the entire imaging system were performed to determine the behaviour of the veiling glare, the uniformity of the spatial sensitivity, and the EPID response with changes in field size and phantom thickness. The veiling glare was caused by several factors: the mirror, the cameras themselves, and the phantom scatter and beam hardening. The magnitude of the glare was spatially dependent. The EPID response was not spatially uniform, but increased by approximately 25% in the region farthest from the screen-mirror junction. The cause of this increase was determined to be the mirror. The dose-corrected EPID response with changes in phantom thickness was nearly flat for medium-sized fields, although it did increase slightly for large fields and decrease slightly for small fields. The overall performance of the CCD camera was found to be significantly better than that of the Newvicon camera. Central axis dosimetry would be straightforward to calibrate; however, the spatially dependent glare observed in the system would make it extremely difficult to deconvolve an EPID image to provide a two-dimensional dose map.

Table of Contents

1 Introduction

Cancer is expected to cause 65 000 deaths in Canada this year, and an estimated 132 100 new cases of cancer will be diagnosed [NC00]. Once cancer is diagnosed, the treatment options include surgery, radiotherapy, and chemotherapy. Often, these are used in combination.

Radiotherapy treatments often consist of irradiating a tumour using photon or electron radiation. Rather than administering one large dose of radiation, it is usually administered in smaller doses over four to six weeks of daily treatments, called fractions. Reasons for fractionation of the dose include allowing time for repair of sublethal damage to tissues; allowing time for the remaining tumour cells to pass through the cell cycle to a more radiosensitive phase; and allowing diffusion of oxygen into the remaining tumour to take place, which will increase the efficacy of the next dose [Ha93]. The macroscopic result is that the normal tissues have time for repair, while the tumour does not, thus separating the two dose-response curves.

During the irradiations, the radiation beam is shaped by collimators and lead blocks so as to deliver adequate dose to the tumour and a surrounding region. This provides a margin of error which should compensate for local subclinical spread, regions with suspected malignant cells, movement of organs within the body, and errors in patient positioning [IC93].

1.1 Need for radiotherapy verification

For many tumour types, dose escalation will result in an increase in tumour control; however, an increased dose also carries an increased risk of normal tissue

complications. The dose prescribed to the patient is chosen carefully so as to balance the probability of tumour control with the probability of normal tissue complications. The International Commission on Radiation Units [IC76] has stated that the dose actually delivered to the patient should be within 5% of the prescribed dose. This accuracy is required because the doses used for patient treatment tend to lie on a steep part of the dose-response curve, and a small change in dose can result in a large change in outcome.

Numerous factors can contribute to the error in administered dose. The International Commission on Radiation Units and Measurements (ICRU) identifies at least four sources of errors in radiotherapy: human mistakes, instrumental mistakes, random errors, and systematic errors [IC76].

> "In principle, mistakes can be eliminated completely by a proper system of checks and cross-checks of both human and instrument performance...Random and systematic errors, on the other hand, cannot be eliminated but the magnitude of these uncertainties can be reduced by the accumulation of better data and improved techniques of measurement and delivery of radiation." [IC76, p. 45]

Since patient treatments are administered over many sessions, it is important to minimize positioning errors, both of the patient and of field shaping blocks and wedges. During the treatment planning phase, a simulation is performed to ascertain that the tumour will be adequately covered by the radiation field. Alignment lasers are used in the simulation and marks are made to indicate the position of the lasers on either the patient's skin or on a cast used for immobilization. These marks can then be used with the lasers in the treatment room to align the patient with the treatment field. Ideally, the patient would then be correctly positioned for each treatment. Centralized computer systems exist for the storage of treatment parameters and once entered, they would not be changed for the course of the treatment.

However, in practice, errors resulting in doses deviating by more than 5% from the prescribed dose have been documented by various authors [Mi91, Le92a, Le92b, Ca93, No95]. These errors have their origins in different parts of the treatment process, but the authors have concluded some of the errors could have been detected and rectified by using a portal imaging device, *in vivo* dosimetry, or a combination of both [Mi91, Le92a, Le92b, No95].

1.2 Portal imaging

1.2.1 Overview

Portal imaging encompasses a variety of techniques used to gather an image during a radiation treatment. The treatment field is also known as the treatment portal, which gives portal imaging its name.

A variety of portal imaging techniques make use of film. A film/screen combination is placed on the exit side of a patient during a radiation treatment. In a localization radiograph, an image is acquired during the first few monitor units of irradiation; in a verification radiograph, a less sensitive film is left in place for the entire treatment; and in a double-exposure radiograph, the film is exposed to a few monitor units of a large field, followed by the remaining monitor units using the treatment parameters. These types of radiographs are limited in their usefulness, mainly because the results are not available in real-time. They suffer from poor contrast and spatial resolution. In addition, quantitative use of the films is difficult, and the use of films incurs high costs in terms of both equipment and time spent developing the films. [Sh95]

A number of on-line portal imaging systems have been developed. These systems are meant to acquire and display an image in real-time. To differentiate on-line portal imaging systems from film, they are referred to as electronic portal imaging systems, or EPIDs. An overview of EPIDs commonly in use is given by Shalev [Sh95].

Solid state detectors make use of diodes or MOS-FETs (metal-oxide semiconductor field effect transistors) as radiation detectors. Shalev [Sh95] describes a linear array of silicon diodes, first constructed by Lam *et al.*, which can be physically moved (scanned) across the radiation field to produce a two-dimensional image. Scintillating crystals coupled to photodiodes, again organized in a line, can also be used to scan across a radiation field; Shalev [Sh95] discusses this technique, which was first developed by Morton *et al.* However, scanning across the radiation field is a slow method of acquiring an image. Shalev [Sh95] describes one solution to this problem, which was developed by Antonuk *et al.* A multielement amorphous silicon detector array (MASDA) consists of photodiodes which are coupled to transistors and placed in contact with a metal/phosphor converter plate.

Instead of solid state devices, a scanning liquid ionization chamber, or SLIC, can be used to acquire a portal image. Shalev [Sh95] explains this technique, which was first developed by Van Herk and Meertens. A matrix ionization chamber is filled with isooctane and covered by a 1-mm thick steel plate. The charge in individual chambers is read out by controlling the voltages of the chambers.

Of the commercially available types of EPIDs, video-based EPIDs are still the most commonly types seen in clinical use [Mu95]. This type of portal imager is the focus of this thesis and is described in detail in Section 1.2.2below.

1.2.2 Introduction to video-based portal imaging

In video-based portal imaging, the detector consists of a metal/phosphor screen combination which is placed at some distance from the exit side of the patient, and converts the megavoltage radiation into visible light. The light produced by the screen is reflected from one or more mirrors and viewed by either a tube-based video camera or a charge-coupled device (CCD) camera. The camera is interfaced with a computer which digitizes the signal received from the camera and displays the image on a monitor. Among the commercially available EPIDs are Theraview (Cablon Medical BV), BEAMVIEW^{PLUS} (Siemens Oncology Systems), and SRI-100 (Philips Medical Systems) which has now been remodeled as *i*View (Elekta Oncology Systems Ltd.).

The metal/phosphor screen serves several purposes. The metal keeps the scattered electrons and lower-energy scattered photons from reaching the phosphor screen. It provides buildup so that the screen will receive a higher dose than it would without buildup; this, in turn, results in a higher light output from the screen. Imaging properties of different thicknesses of both metal and phosphor have been investigated [Wo94]. Commercial video-based portal imaging systems use steel or brass plates ranging in thickness from 1.3 mm to 2.0 mm, along with gadolinium oxysulfide (Gd_2O_2S) phosphor screens of thicknesses ranging from 160 mg/cm^2 to 411 mg/cm^2 [Mu95].

At least one mirror is necessary because the camera will suffer increased noise, as well as radiation damage, if it is directly exposed to the radiation beam. Some systems use a single mirror placed at 45° to the optical axis, while other use two mirrors, both placed at 45° to the optical axis. The mirror and camera are enclosed in a light–tight apparatus.

1.2.3 Tube-based video cameras

The heart of a tube-based video camera is a tube whose photosensitive surface is a photoconductive layer. Camera tubes come in different sizes and types. The tube sizes are classified by the diameter of the tube in inches. The commonly available tube sizes are 1/2", 2/3", and 1". There is a relationship between tube diameter and size of the photosensitive area: one-half of the tube diameter is equal to the length of the longer side of the rectangular photosensitive area. The tube types are specialized for different applications, and each type has its own proprietary name [NA99]. Different tubes have different resolutions, contrast, and "lag" (a time constant describing the sensitivity of the photosensitive surface).

The most common type of tube in everyday medical applications is the Vidicon tube. Its resolution and lag are better than average [NA99]. The types of tubes used in commercial video-based portal imagers include Plumbicon or Chalnicon (TheraView) and Newvicon (BEAMVIEW^{PLUS}) [Mu95]. The Plumbicon, developed by Philips, is characterized by better-than-average resolution, lag, and signal-to-noise ratio. The Newvicon, a registered trademark of Matsushita, has a high light sensitivity, and its spectral response extends into the infrared range. The Chalnicon, produced by Hamamatsu, is characterized by high sensitivity in the visual spectrum, although it demonstrates more lag than a Newvicon [NA99].

A tube camera has a 4:3 aspect ratio. It operates in "interlace mode", meaning that every second line is read out in a raster pattern, and then the lines in between the first set are read out in a raster pattern offset by one line relative to the first. All these lines

together constitute one frame. It should be noted that because of interlacing, adjacent lines in a frame are separated in time by one-half the readout time of the camera.

The cameras generally operate in RS-170 mode, which is a protocol defined by the EIA (Electronics Industries Association) specifying the nature of synchronization signals used by the camera [DB99a]. Alternatively, the European standard is known as CCIR (Comité Consultatif International des Radiocommunications). The differences between the two standards lie in the frame rates and lines of resolution. Both standards use interlacing, which reduces flicker [DB99a]. RS-170 mode and its colour counterpart, RS-170a (known as NTSC and used for standard television transmission) transmit 525 lines per frame at 30 frames per second. CCIR transmits 625 lines per frame at 25 frames per second. Of the lines transmitted, some are used for synchronization signals, so that the number of visible lines is 485 for RS-170 and 575 for CCIR [DB99a].

The size of tube dictates the type of lens used with the camera. The lenses are threaded so that they can be screwed in to a standard camera mount. There are different mounts which result in different distances between the lens and the imaging surface.

1.2.4 Charge-coupled device (CCD) cameras

A charge-coupled device (CCD) has a photosensitive semiconductor surface divided into an array of light sensitive elements (pixels). Light striking the surface of the chip produces electron-hole pairs. Applied potentials trap the electrons, and the charge accumulated in each pixel is read out in an orderly fashion through an amplifier. A shutter, mechanical or electronic, blocks the light to the chip during the read-out. The time during which charge is allowed to accumulate on the CCD is referred to as the integration time.

CCD chips are made in sizes which are compatible with standard video tube sizes, as well as some smaller sizes. Currently, the available sizes are 1/4", 1/3", 1/2", 2/3", and 1". The chips can be constructed with different numbers of pixels. For a given chip size, a higher number of pixels increases the resolution, but it also increases the readout time per frame. Lenses with standard video mounts are available in each of the different sizes.

A typical CCD camera is designed to read out in RS-170 or CCIR format. A camera which reads out at a non-standard frame rate will need a specialized frame grabbing board. A *slow-scan* CCD camera is one which collects frames at a slower rate than the video standard. This is the type used in video-based portal imaging, because of the greater flexibility allowed by user-controlled integration times.

A CCD with a shutter has to block incoming light to its sensitive area while the image is being read out. This leads to a delay between frames which is related to the number of pixels being read out. An alternative to this type of CCD is a *frame-transfer* CCD, which has its sensitive area divided into two sections. One section is the imaging array, and the other section is covered with an opaque mask and is called the storage array. Charge can be transferred from the imaging array to the storage array in as quickly as a few microseconds so that charge accumulation can begin again almost immediately. While the next frame is collected, the current frame is read out into the computer.

The *full well capacity* is the maximum number of electrons which can be accumulated in each pixel. Even without light falling on the chip, thermally generated charge accumulates in the CCD. This charge is called *dark current*. One minute in the dark at room temperature may be enough to fill the CCD chip to its full well capacity [DB99a]. The dark current can be greatly reduced by cooling the chip. For astronomical

observations, where long integration times of 60 s or more are required, cooling is necessary; however, the integration times used in portal imaging are on the order of 250 ms, so cooling the CCD is unnecessary.

Bias level refers to the electrons present when the CCD chip is set to zero integration time. A *bias frame* is a frame acquired with no light present and zero integration time. *Gain* or *CCD conversion factor* is a measure of the number of electrons which correspond to one analog-to-digital unit (ADU) or greylevel.

1.2.5 Lenses

Most camera lenses are actually compound lenses, consisting of two or more lenses permanently mounted in a specific configuration. There are various parameters to consider when selecting a camera lens. The first consideration is the tube size. Lenses are designed to be compatible with standard tube sizes; therefore, a 1" lens is used with a 1" tube (or 1" CCD chip). It is possible to use a lens which is a larger format than the tube [DB99b]; however, it is not recommended to use a lens which is a smaller format than the tube, since it will cause severe *vignetting* (see below) [Po99].

The next parameter to consider is focal length, which is generally expressed in millimetres. The types of mounts available on lenses, in combination with the construction of the cameras, conform to certain standards so that the distance from the lens to the imaging surface is always the same for a given format of lens. This, in turn, determines the angle of view of the camera, which determines the field of view at a given distance from the camera. In addition, the focal length and format of the lens determine the *minimum object distance*. Any image closer than the minimum object distance will not be focussed onto the imaging surface [Po99].

A third parameter is the F/# or *f*-stop of the lens. All lenses have an iris diaphragm or aperture which can be adjusted to let more or less light into the camera, as the situation dictates. The *f*-stop quoted on a lens is a measure of the largest opening possible for the lens aperture, and is defined as

$$\text{F/\#} = \frac{f}{D} \qquad \text{Equation 1 [Hec74]}$$

where f is the focal length and D is the diameter of the lens opening. The lower the *f*-stop, the larger the diameter, and the more light is allowed into the camera. The usual sequence of *f*-stops on a lens is 1.4, 2.0, 2.8, 4.0, 5.6, 8.0, 11.0, 16.0. Each increase in F/# results in a doubling of light intensity reaching the camera. [Hec74]

The aperture size has an effect on the spatial distribution of the light intensity reaching the camera. For a pinhole aperture, the intensity of light falling on the photosensitive surface is uniform across the surface. As the aperture is opened up, the light intensity near the edges of the photosensitive surface can decrease drastically compared to that falling on the optical axis; this is referred to as *vignetting*. It is caused by the rims of the lenses and apertures which make up the optical system. [Hec74]

1.3 Dosimetry using video-based portal imaging

In the last several years, researchers involved in video-based portal imaging have been aware of the possibilities of using an EPID for portal dosimetry. If an EPID were calibrated to measure dose, the two-dimensional dose map available from the EPID could be compared to the dose predicted from the treatment planning system [Sh95, Sh96]. Progress on this problem has been made by several groups worldwide.

1.3.1 Previous research

At the Dr. Daniel den Hoed Cancer Center, Rotterdam, the Netherlands, the prototype for the original Philips SRI-100 was developed by Visser *et al.* in the late 1980s [Vi90]. This EPID used a CCD camera (256 x 512 pixels) permanently mounted on the gantry of a 6-MV linear accelerator. Originally, the spatial and contrast resolution were studied, along with evaluation of the ease of use and interference in patient treatment. In addition, the possibility of using the EPID in day-to-day clinical situations was studied, and they concluded that the time and convenience of the EPID were such that day-to-day use was feasible. [Vi90]

By 1993, a group led by Kirby at the North Western Medical Physics Department, Manchester, England, was investigating measurement possibilities using an EPID [Ki93]. The EPID used was again the Philips SRI-100. Techniques were developed to assess the reproducibility of a multileaf collimator (MLC) system, as well as to determine *in vivo* exit doses. For the MLC measurements, a calibration curve of the dose across the edge of a collimator leaf was measured; the leaf was then moved away, repositioned, and its position determined by interpolation in the calibration curve. Exit doses were determined by first taking a set of calibration measurements at different phantom thicknesses and exit distances, and then interpolating in the calibration curves to find the dose for a given measurement. They found the system to respond linearly with dose, with sufficient dynamic range to resolve individual monitor units. Under a restricted set of conditions, they used the EPID to measure exit doses which were in agreement within 2.5% with actual exit doses. [Ki93]

In 1995, Dirkx and others from the Dutch group used the SRI-100 for daily dosimetric quality control of a MM50 Racetrack Microtron [Di95]. The EPID was used to image several open beams and one wedged beam, and its output was compared with that of an ionization chamber. From repeated measurements over time, they concluded that the EPID could be successfully used for daily quality control. A protocol was written to allow the everyday use of the EPID in this manner. [Di95]

At the same time, Heijmen *et al.*, also of the Dutch group, were using the EPID to measure portal doses [Hei95]. The response of the EPID with increasing thickness of absorber in the beam was investigated. They found that the greylevel values were proportional to dose, and the constant of proportionality was independent of phantom thickness; however, it was dependent on field size. They determined that the change in EPID response with field size was due to scattering of light photons within the EPID apparatus. [Hei95]

In 1995, Kirby reported using their EPID for both exit dosimetry and quality control measurements [Ki95]. They found that the central axis exit doses agreed with silicon diode measurements within 3%, and the field flatness measurements agreed with Farmer chamber measurements within 1.5%. In addition, segmented intensity modulated fields were verified using the EPID. [Ki95]

Measurements of noise in the SRI-100 system were made by Althof *et al.* of the Dutch group [Al96]. They found that camera read-out noise was the limiting factor in the visibility of structures for low doses, and they proposed that a new frame-transfer CCD be used in the place of the original CCD camera, which read out in standard video mode. [Al96]

Pasma *et al.* of the Dutch group have made portal dose measurements for both open and wedged beams as well as dynamic multileaf collimation [Pa98]. A convolution algorithm was applied to correct for glare, non-uniform spatial response, and nonlinearities present in the EPID, and doses were calculated from EPID images. Comparisons were made with ionization chamber measurements, and the agreement was found to be within 1%. [Pa98]

At the University of Manitoba, Rajapakshe performed an in-depth study of the optimization of a portal imaging system for quantitative imaging [Raj95]. System noise was addressed in detail and methods were applied to minimize the noise. Several cameras were compared to assess their suitability for quantitative imaging, and a cooled CCD camera was found to work best. Preliminary investigations into measurements of exit dose were carried out, and an accuracy of better than 3% was achieved. [Raj95] Later, Fielding [Fi98] developed software to allow greater flexibility in data acquisition with clinical portal imaging system. In addition, further calibration measurements necessary for dosimetry were begun [Fi98].

1.3.2 Current work

Previous investigations of portal imaging systems have only given a cursory examination to camera characteristics. However, the quality of the camera and associated hardware has a great effect on whether images produced will be acceptable for medical purposes. The linear accelerators used in patient treatment are pulsed at a frequency comparable to the frame rate of a standard video camera, and pulsation artifacts are just one of the many drawbacks of using a conventional video camera in a portal imaging device. [Raj95] Certainly any quantitative use of the portal imager should be preceded

by a thorough examination of camera characteristics. Optical properties of the imaging chain which can affect image quality independent of camera effects should also be investigated.

There is currently a great deal of interest in the use of EPID images to provide exit dose maps. To relate the EPID greylevels to exit doses, the image must be deconvolved to account for cross-talk effects in the EPID. However, the calculation will only be realistically achievable if the kernel describing the cross-talk effects is spatially invariant. Therefore, the spatial variation of the optical properties must be investigated.

The focus of the current work will be a comparison of two cameras used in electronic portal imaging with a particular emphasis on their suitability for exit dose measurements. The first camera, a Newvicon camera, is the camera currently supplied as part of the Siemens BEAMVIEW^{PLUS} system. The frame-grabber along with custom-written data acquisition software will be used to acquire and store images. The second camera is a custom-built CCD camera (Electrim Corporation), interfaced to a computer and data acquisition software. Tests will be carried out on the cameras themselves as well as individual segments of the imaging chain to assess the response of the system to radiation or light input at each stage.

2 Materials

2.1 Siemens Mevatron and BEAMVIEW^{PLUS} system

All measurements were made on a Siemens Mevatron MX2 linear accelerator, using a photon energy of 6 MV. The Siemens portal imaging apparatus, a BEAMVIEW^{PLUS} system, was attached to this machine. The experimental apparatus used to test the cameras was based on the BEAMVIEW^{PLUS} design, so a brief overview of the BEAMVIEW^{PLUS} system will be presented here.

The BEAMVIEW^{PLUS} system was designed to mount on the gantry, and it can be retracted into the gantry when not in use, or when its use would interfere with patient treatment. It consists of a brass plate in direct contact with a Kodak Lanex Fast Back phosphor screen. The phosphor/screen combination is situated at a source-to-surface distance (SSD) of 139 cm. When the EPID is in its extended position, the Newvicon camera inside the gantry views the screen using a front-silvered mirror positioned at 45° to the beam. The distance from the front of the lens to the screen is 112 ± 2 cm. For a diagram of the apparatus, see Figure 2-1.

The brass thickness has been measured as 1.30 ± 0.01 mm (1.108 ± 0.009 g/cm^2). The phosphor is composed of gadolinium oxysulfide (Gd_2O_2S) of 0.63 ± 0.02 mm thickness (0.221 ± 0.007 g/cm^2). The total density thickness of the brass/phosphor combination is 1.33 ± 0.01 g/cm^2.

The camera is interfaced to a Unix-based workstation (SPARC CPU-2ce) which is equipped with frame-grabbing hardware (single double-height VME bus card with ICS-225 Device Driver Real-Time Image Processor), capable of 8-bit digitization at a

rate of 30 frames per second. A 16-bit arithmetic logic unit (ALU) allows for real-time frame averaging.

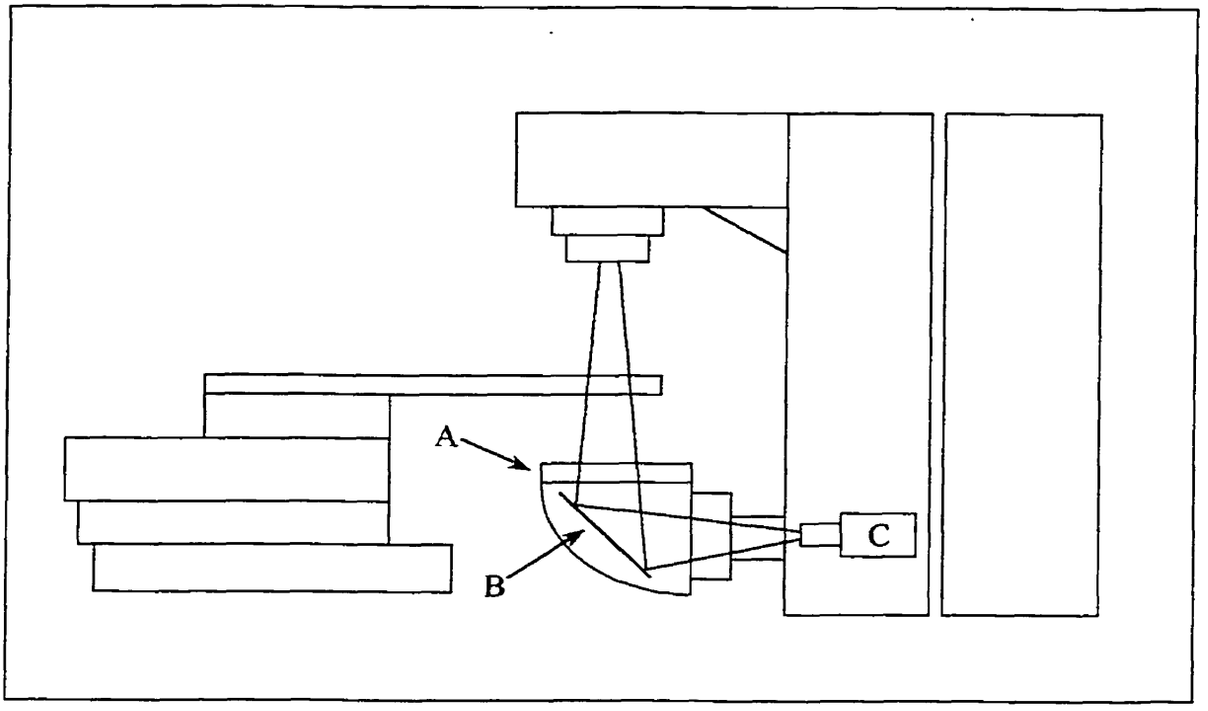

Figure 2-1 Diagram of the BEAMVIEW^{PLUS} portal imaging system. Radiation strikes the metal/phosphor screen (A), which converts the radiation to light. The light from the screen reflects from the mirror (B) into the camera (C).

2.2 The light-tight box

Experimental apparatus designed to simulate the BEAMVIEW^{PLUS} system was constructed by the in-house machine shop to obtain the data discussed in this practicum. It consists of a wooden box (39 cm wide x 153 cm long x 37 cm deep) with a hinged lid to allow access to the cameras inside. The top of the box is 91 cm from the floor, resulting an SSD of 138.5 cm, very close to that of the BEAMVIEW^{PLUS} system. It is painted black inside to reduce unwanted reflections, and made light-tight by the use of

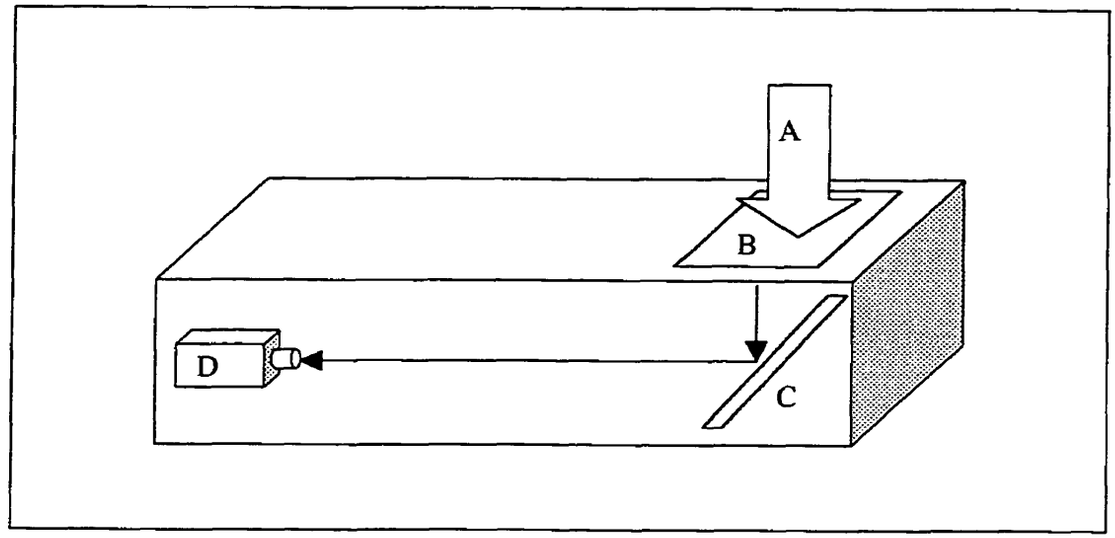

Figure 2-2 Schematic diagram of the light-tight box used in the camera tests. Radiation (A) strikes a metal-phosphor screen (B), and the light from the screen is reflected from a mirror (C) into a camera (D).

foam around the edges. Two latches allow the box lid to be tightened down against the foam to ensure the light-tightness.

The camera mount is situated at one end of the box. At the other end of the box is a 45° front-silvered mirror (37 cm x 47 cm). Above the mirror is a rectangular hole which can hold either a brass plate with an attached phosphor screen for the radiation field measurements, or a piece of plastic supported by a frame for the light field measurements. The phosphor screen, 43.2 cm wide by 35.6 cm long, is centred on and affixed to the 45.6 cm x 38.0 cm brass plate. Figure 2-2 shows a diagram of the light-tight box.

The box is equipped with locking wheels which allow for positioning of the box as desired in the beam, and also allow for removal of the box from the treatment room during clinical hours.

One camera at a time can be mounted in the box on a metal arm. This arm also allows for adjustment in height of the cameras, and some adjustment in the distance of

the cameras from the mirror. The design of the mounting arm somewhat limits the positioning of the cameras so that during measurements, the two cameras were situated at slightly different distances from the mirror. The distance from the front of the lens to the mirror, along the camera's optical axis, was 85 ● 1 cm for the Newvicon camera and 95 ● 1 cm for the CCD camera. The distance along the optical axis from the mirror to the screen was 16 ● 1 cm, for a total imaging distance of 101 ± 1 cm for the Newvicon camera and 111 ± 1 cm for the CCD camera, comparable to that in the original BEAMVIEW^{PLUS} system, which was 112 ± 2 cm.

When taking radiation measurements with the CCD camera, 5 cm of lead shielding was placed around the camera to reduce the noise as well as the potential damage to the CCD chip. Because it is less sensitive to scattered radiation, the Newvicon camera was not shielded during radiation measurements.

The Kodak Lanex Fast Back phosphor screen, supposedly identical to the one used in the BEAMVIEW^{PLUS} system, is 0.56 ● 0.01 mm thick. Using a density of 3.5 g/cm^3 [Rad93], this translates to a density thickness of 0.196 g/cm^2. The brass plate is 1.60 mm thick, and using a density of 8.5 g/cm^3 for the brass [Ke81], this translates to a density thickness of 1.36 g/cm^2. The total density thickness of the metal/screen combination is 1.56 g/cm^2. The brass plate in the light-tight box is slightly thicker than that in the BEAMVIEW^{PLUS} system, while the phosphor screen is slightly thinner (see Section 2.1). However, the depth of maximum dose (d_{max}) for the MX2 6 MV photon beam is 1.5 cm, and thickness of the metal/phosphor screen combination for both systems is near this depth, where the depth-dose curve is relatively flat. Therefore, in spite of the differences in thickness, a similar response was expected from the two systems.

For measurements using the visible light field, the metal/screen combination was replaced with a piece of white translucent plastic supported by a frame. This was illuminated by a small (1 cm diameter) incandescent light bulb attached to the ceiling, at a distance of 179 ± 2 cm. To achieve a variety of different light levels, several bulbs of different brightnesses were used over the course of this experiment, powered by several different DC power supplies. Measurements made with a radiometer (International Light IL 730A U. V. Actinic Radiometer) at different positions on the plastic screen showed that the resulting light field was uniform to within 3% on the incident side of the plastic over the field of view of the camera. The light measurements were carried out in a darkened room.

2.3 The light box

Several measurements were made using a light source which the cameras viewed straight on, as opposed to using the 45° mirror. A light box apparatus which had a small gantry for mounting cameras at a variable distance was adapted for use with these particular low-light cameras. See Figure 2-3 for a schematic diagram.

The light box consists of a small light bulb inside a metal box 41 cm long by 34 cm wide by 30 cm deep (*Illuma System* by Bencher, Inc.). The metal box was painted with white reflective paint inside. The light bulb itself was shielded from directly illuminating the camera by a diffuser plate. A piece of white plastic was mounted on the opening to the box, so that a light field was created which was uniform within 3%, as measured with a radiometer. The camera viewed this white "screen" directly from above. An additional piece of plastic could be placed on top to attenuate the light further.

It was found that the original light (120V, 600W) included in this apparatus was so bright that not only were the cameras saturated, but they ran the risk of being permanently damaged. Therefore, the original light bulb was removed and a dimmer one (24V, 90 mA bulb powered by a 12V power supply) was placed in the same position within the box. The measurements were taken in a very dark room.

To obtain the same distance from the light screen to the camera as in the light-tight box measurements, the camera focus was left at the position appropriate for use in the box with the mirror. The camera was attached to the gantry of the light box, and the distance to the screen was adjusted until its image was once again in focus. The camera-screen distance was then the same as in the light-tight box.

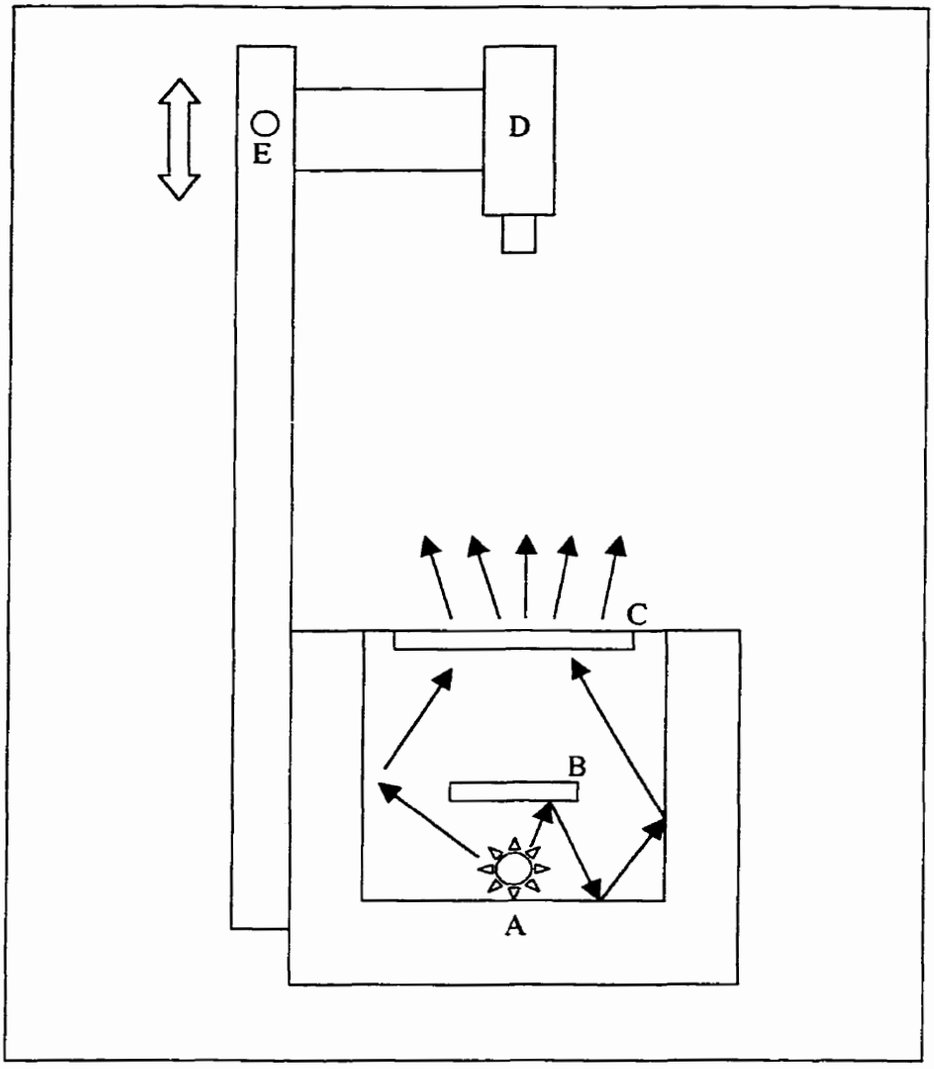

Figure 2-3 Schematic diagram of light box used for measurements not involving the mirror. A light bulb (A) is placed in a box with a reflective interior. Light reflects from the interior of the box but also the diffuser plate (B), passes through a white plastic screen (C), and strikes the camera (D). The camera's distance from the screen is adjustable (E).

2.4 Newvicon camera and data acquisition

The Newvicon camera has a 1" format tube and is equipped with an F/1.1 37.5-mm focal length lens. This camera was the backup camera for the clinical BEAMVIEW^{PLUS} system, so the camera was identical to that in the clinical system. The images, 512 x 480 pixels, cover an area of 30.1 cm x 23.9 cm at the EPID surface.

Further details of the Newvicon camera and optics are summarized in Table 1. Automatic gain and black level control was disabled for this work; instead, the gain and black level were always set manually. The lens aperture was always set at its largest opening of F/1.1, because the low light levels involved in portal imaging required as much light as possible to be captured by the camera.

The clinical BEAMVIEW^{PLUS} system was disconnected from its computer for these measurements so that its computer and frame grabber board could be used for the data acquisition. The RS-170 output from the camera is sent to the clinical computer, which was controlled by software written specially for this purpose[1]. Frame averaging takes place at two levels. First, 32 consecutive RS-170 frames are digitized and averaged to create a single 8-bit "frame". Second, the averaged 8-bit frames are summed in a frame buffer to produce a 16-bit image. The acquisition of frames is triggered by a "beam-on" signal from the linear accelerator; therefore, the number of frames added to produce the 16-bit image is determined by the beam-on time. When light field data were acquired, a manual switch was used to simulate the beam-on signal for the purposes of starting and stopping the acquisition. The number of frames and other pertinent image details are recorded by the software in a separate header file.

2.5 CCD camera and data acquisition

The imaging surface of the CCD camera is a 2/3" Texas Instruments TC-217 frame-transfer chip. The camera itself was custom-built (Electrim Corporation, Princeton, NJ). It is interfaced to the computer via a specially designed PCI interface board (Electrim Corporation). The camera settings such as integration time, frame

[1] The acquisition program was written by Dr. Harry Fielding.

averaging, gain, and bias are controlled by the user with the software supplied with the camera. The signal from the camera is digitized to 8 bits, and the camera is capable of integrating up to 128 frames, resulting in a 16-bit image which is saved to disk. The image size is 1134 x 486 pixels, which results in a field of view of 39.7 cm x 29.6 cm at the EPID surface. The camera is equipped with a 2/3" F/1.6 25-mm lens which has locking screws for the focus and aperture settings. Again, the aperture was always set at its lowest setting of F/1.6. Further details are summarized in Table 1.

		Newvicon	CCD
Format		1"	2/3"
Imaging sensor		Newvicon S-4076	Texas Instruments TC-217
Output		RS-170	Non-standard
Lens		Kowa TV F/1.1, 37.5mm	Tamron high-resolution F/1.6, 25 mm
Image dimensions (pixels)		512 x 480	1134 x 486
Image dimensions (cm)	**EPID surface**	30.1 x 20.9	39.7 x 29.6
	Isocentre	21.7 x 17.3	28.7 x 21.4
Pixel size (cm)	**EPID surface**	0.059 x 0.050	0.035 x 0.061
	Isocentre	0.042 x 0.036	0.025 x 0.044
Dimensions of a 1cm^2 ROI (pixels)		18 (H) x 30 (V)	28 (H) x 16 (V)

Table 1 Summary of camera characteristics for the Newvicon and CCD cameras

2.6 General procedures

2.6.1 Alignment, focussing, pixel size

The alignment of each camera was checked before it was used to acquire data in the light-tight box. The difference in sizes of the two cameras required repositioning of the mount arm up or down, depending on which camera was being used. The "BEAMVIEW^{PLUS} test screen", included for use with the BEAMVIEW^{PLUS} system and shown in Figure 2-4 was used to help centre the cameras. It was mounted on the frame

used for light measurements, and the camera was moved until it was centered as accurately as possible on the screen.

To focus the camera, a sheet of paper containing four groups of line pairs (spaced at 0.15 lp/mm, 0.24 lp/mm, 0.60 lp/mm, 1.18 lp/mm) was attached to the side of the BEAMVIEW^{PLUS} test screen nearest the camera. The camera focus was then adjusted until the greatest number of line pairs per millimetre was resolved; for both cameras, the 0.60 lp/mm group was the greatest resolution possible. The focus was then fixed, using masking tape in the case of the Newvicon camera, and using the set screw in the case of the CCD camera.

The pixel size was determined by acquiring an image of the BEAMVIEW^{PLUS} test screen. The spacing of grid lines was known to be 5 cm in both the horizontal and vertical directions. By measuring in pixels the distance between grid lines in an image of the BEAMVIEW^{PLUS} test screen, the pixel size was determined.

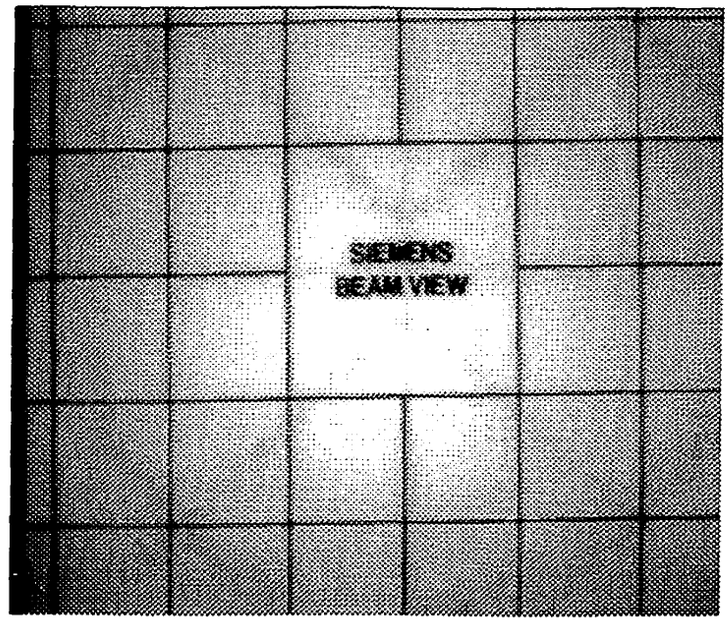

Figure 2-4 The BEAMVIEW^{PLUS} test screen

2.6.2 Curve fitting

All curve fitting was performed using MicroCal Origin, a software package designed for scientific data analysis. This program used the Levenberg-Marquardt method to fit the data. The Levenberg-Marquardt method is a least-squares method which minimizes the value of chi-squared (χ^2). The uncertainties in the fitting parameters correspond to the change in the value of the parameter which produces a change of 1 in the value of chi-squared.

2.6.3 Background subtraction

Background measurements were subtracted from every data set which was analyzed. For radiation measurements, the background measurement was an image acquired with the beam off. For light measurements, the background measurement was an image acquired with the main light source off.

For the Newvicon camera, it was impossible to acquire a predetermined number of frames, because the number of frames did not depend very precisely on the time the beam-on switch was active. Therefore, a background acquisition of 128 frames was taken, and divided 128 to obtain a single background frame. It was used to correct subsequent images in one of two ways. For light field images, only the greylevel per frame was of interest, so the image itself was divided by the number of frames and the background was subtracted. For radiation field images, the total greylevels were of interest, so the background image was multiplied by the number of frames in the image to be corrected, and then it was subtracted. Each day that data were taken, a background image was acquired, in case there were any day-to-day variations in the background signal present.

For the CCD camera, since the number of frames acquired was controlled by the software, it was much simpler to acquire background measurements with the same integration time and same number of frames as the data, and subtract them directly. Therefore, if images with different integration times or different numbers of frames were acquired on a given day, one background data set was taken for each.

2.6.4 Centre-finding routine

For all images involving square or circular fields, whether of light or of radiation, it was necessary to compute the mean greylevel in a region of interest in the centre of the field. Rather than visually examining the images to determine their centres, a software routine was written to find the centre of a given image.

First, the background was subtracted from the image, and a correction was made for lens vignetting (see 4.1.4). Then, the software routine used a "centre-of-mass" method to find the centre of the bright region representing the square or circular field.

For a physical object made up of n particles of mass m_i located at positions $\vec{\mathbf{r}}_i = x_i\hat{\mathbf{i}} + y_i\hat{\mathbf{j}} + z_i\hat{\mathbf{k}}$, the position $\vec{\mathbf{R}} = X\hat{\mathbf{i}} + Y\hat{\mathbf{j}} + Z\hat{\mathbf{k}}$ of the centre of mass is calculated using

$$\vec{\mathbf{R}} = \frac{\sum_n m_i \vec{\mathbf{r}}_i}{\sum_n m_i}$$

Equation 2

or, in component form,

$$X = \frac{\sum_n m_i x_i}{\sum_n m_i}$$

$$Y = \frac{\sum_n m_i y_i}{\sum_n m_i}$$

$$Z = \frac{\sum_n m_i z_i}{\sum_n m_i}$$

Equation 3

Equation 4, constructed in analogy with Equation 3, was used to determine the centre of mass of the image. The greylevel value for each pixel replaced the mass in Equation 3, and the sum was performed over the x and y coordinates, in pixels, of each pixel in the image.

For a greylevel g_i in a pixel (x_i, y_i), the following sums were computed to give the centre of mass (X,Y):

$$X = \frac{\sum g_i x_i}{\sum g_i}$$

$$Y = \frac{\sum g_i y_i}{\sum g_i}$$

Equation 4

A threshold was used to exclude from the sum the points outside the illuminated area. Without the threshold, the centre found by the routine did not always agree with that found by visual examination of the image. The disagreement was sometimes as bad as 100 pixels or more in the x or y direction, or both. It seemed that in spite of the background subtraction, enough of a gradient sometimes remained in the dark areas of the image to skew the results. The threshold was introduced into the calculation to exclude the pixels outside of the bright region. It was then adjusted until the coordinates calculated by the routine agreed within one or two pixels with those estimated by viewing the image. The routine was thoroughly tested on various types of images from the

different sources used in the experiments. The final value for the threshold, which worked well for all the images studied, was set by the software at 20% of the maximum pixel value in the image.

2.6.5 Dosimetry

For some measurements, it was necessary to measure the dose at the EPID surface using an ionization chamber. A Farmer ionization chamber (PTW-Freiburg Type 30001, 0.6 cm^3) was placed in a 30 cm x 30 cm x 2.5 cm polystyrene phantom at a depth of 1.5 cm. Pressure and temperature readings were recorded. All other aspects of each experiment (field size, phantom thickness, phantom position) were kept identical to the conditions of the EPID measurement.

The phantom was placed on top of cardboard boxes or Styrofoam so that the centre of the ionization chamber was as close as possible to the source-to-detector distance of 138.5 cm. Obtaining this distance precisely was sometimes impossible. In practice, the actual distance varied from 139.5 cm to 137 cm. The main source of error introduced by this variation would be due to the $1/r^2$ effect, which would be ± 2% ; the primary and scatter components of the beam should remain relatively the same at these distances. Therefore, a correction was not made for the slight variation in distance.

3 Procedures and Results

3.1 Camera tests

To compare the camera characteristics, some basic tests were performed on both cameras. Abbott [Ab95] wrote a comprehensive document outlining various tests to be performed on a CCD camera. The tests were adapted where possible for use with the Newvicon camera, so that comparisons could be made between the two. Tests were carried out to investigate the linearity, frame grabber effects, noise, clamping, and lens vignetting properties of both cameras.

3.1.1 Linearity

A different test of linearity was used for each camera, due to practical limitations of the equipment available. The behaviour of the Newvicon camera with changes in light intensity was investigated. For the CCD camera, the camera response with changes in integration time was measured.

3.1.1.1 Newvicon camera

To test the linearity of the Newvicon camera with increasing light intensity, a set of neutral density filters was employed. A holder was designed to hold the neutral density filter flush against the front of the lens. The neutral density filters had optical density values ranging from 0.1 to 2.0. The optical density OD and the transmittance T are related by:

$$OD = -\log_{10} T$$
$$T = 10^{-OD}$$

Equation 5

Equation 5 was used to convert the optical density of a filter to its transmittance.

The light-tight box was used in these measurements, with the plastic screen in place and a small light source on the ceiling. For these measurements only, because of difficulties with getting a weak enough light source, the aperture of the lens was set to F/2.0. However, the range of light levels investigated did extend to the lower light levels observed in clinical situations.

The mean greylevel and standard error in a region of interest (ROI) at the centre of the image was calculated at each light level. The region of interest was a square 1 cm by 1 cm at the detector surface, or 18 x 20 pixels. A plot of the data is shown in Figure 3-1. The data were fit to a straight line, with parameters of the fit shown in Table 2. The highest data point (transmittance = 1.0) was excluded from the fit, because the camera was beginning to saturate at this point.

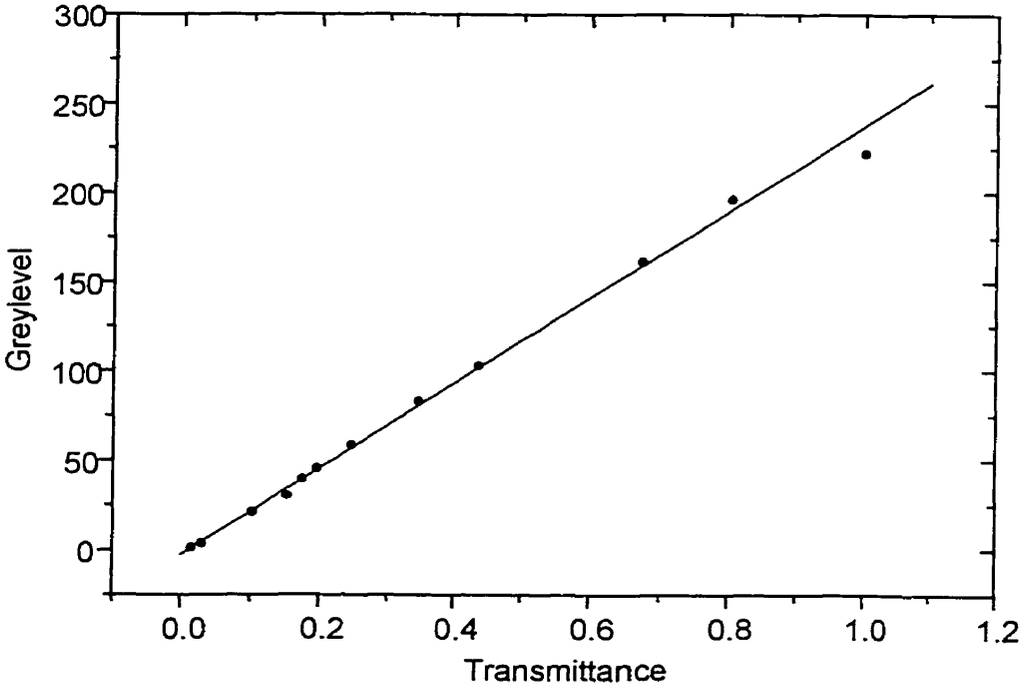

Figure 3-1 Plot of the change in greylevel of the Newvicon camera with light intensity. The last point was excluded from the fit. The error bars are much smaller than the size of the points and thus are not shown. The fit parameters are shown in Table 2.

Camera	Slope (± σ)	Intercept (± σ)	χ^2_v
Newvicon	245 ± 3	-3.0 ± 0.5	6534
CCD	1.912 ± 0.003	26.7 ± 0.1	18.71

Table 2 Parameters of the fits shown in Figures 3-1 and 3-2.

3.1.1.2 CCD camera

The linearity of the CCD camera with increasing integration time was examined. The mean greylevel and standard error were calculated in a 1 cm^2 ROI (28 x 16 pixels) in the centre of the image for different integration times. These times ranged from 0 ms to 150 ms. Above 150 ms, for this particular light source, the camera was completely saturated. Even for the data shown, the last two points begin to show saturation. Examination of the greylevels in the image revealed that the raw image greylevels were

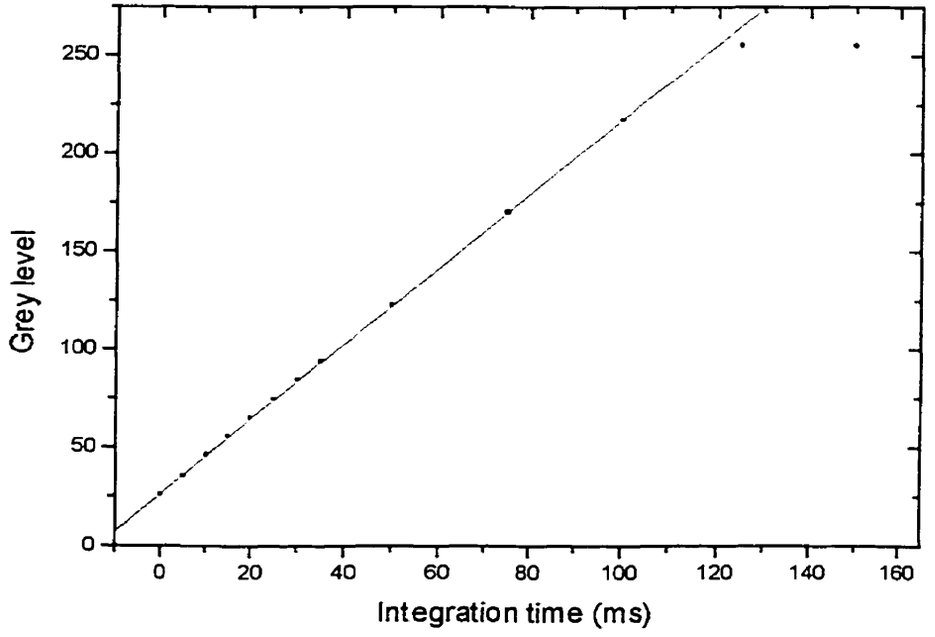

Figure 3-2 Plot of the change in greylevel of the CCD camera with integration time. The last point was excluded from the fit. The error bars are much smaller than the size of the points and thus are not shown. The fit parameters are shown in Table 2.

equal to 255 in the central 8.5 cm of the image at 125 ms, and equal to 255 in the central 24 cm of the image for 150 ms.

A plot of the data is shown in Figure 3-2. The last two data points show where the saturation of the camera begins, and these were excluded from the fit. The parameters of the fit are shown in Table 2.

3.1.2 Frame grabber effects; bias frames

3.1.2.1 Newvicon camera: frame grabber effects

It was observed during data acquisition that the background acquisitions for the Newvicon camera contained a gradient in the vertical direction. Even with the lens cap on, this effect was visible. Figure 3-3 shows a profile in the vertical direction, averaged over the 20 central pixels in a background image; a change of 5 greylevels near the "top" of the image is clearly visible.

To determine if this nonuniformity originated from the camera tube or the frame grabber, a signal generator which was capable of producing a variety of television signals was used to produce an input directly into the frame grabber board. The output of the signal generator was first examined with the help of an oscilloscope to ascertain that it was uniform. By viewing the different video lines with the oscilloscope, it was concluded that there was no discernible change in signal level from top to bottom of the image.

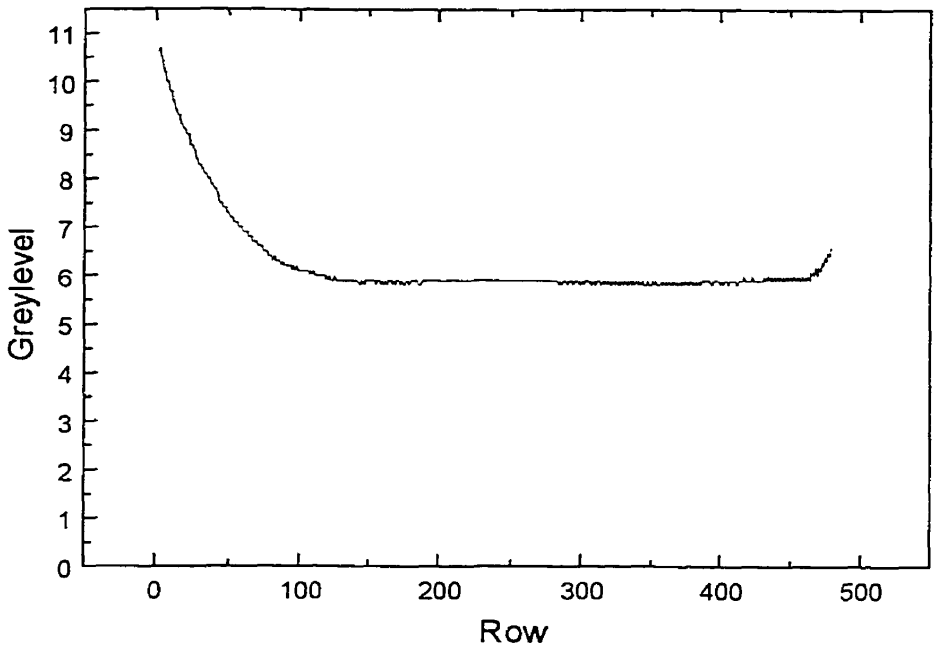

Figure 3-3 Plot demonstrating the nonuniformity in a background image taken with the Newvicon camera.

The signal generator was then used to input a bar pattern, consisting of six vertical bars of different intensities, directly into the frame grabber board. Images of this pattern were acquired and examined for the presence of a gradient. Vertical profiles in each bar were produced, and two are plotted as the lines marked A in Figure 3-4 (a) and (b). The profiles were produced by averaging over 20 columns. A gradient is clearly seen, increasing toward the top of the image. Since the camera was not involved in producing this signal, it can be concluded that the frame grabber must be the source of this nonuniformity.

The lines marked B in Figure 3-4 show the profiles corrected by subtracting background. The maximum difference in greylevels along the uncorrected profiles (A) is 7% for Figure 3-4 (a) and 2% for Figure 3-4 (b). This correction reduces the maximum difference to 3% for the lower greylevels in Figure 3-4 (a) and 0.5% for the higher greylevels in Figure 3-4 (b).

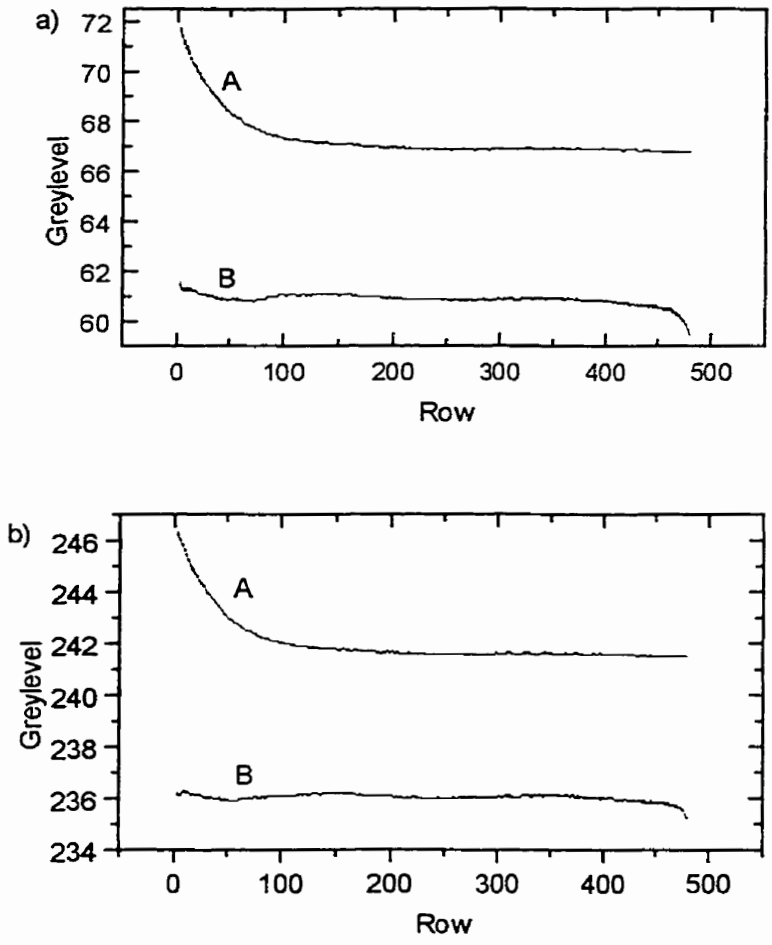

Figure 3-4 Plot of nonuniformity at different greylevels, given a uniform input signal to the frame grabber board (a) for a low greylevel, and (b) for a high greylevel. Lines marked A show the raw background data, while lines marked B show the background-corrected data.

3.1.2.2 CCD camera: delay between frames

In spite of the fact that the CCD chip is a frame-transfer chip, a delay was observed between consecutive frames when acquiring a series of more than one frame. Using a stopwatch, a crude estimate was made of this delay, which appeared to be

independent of integration time. Table 3 shows a summary of the measurements and results.

The maximum readout rate on the specification sheet for the TC-217 chip is 1.2 MHz [TI96]. The readout time for 1134 x 486 = 551124 pixels at this maximum readout rate would be 459 ms, which is approximately equal to the measured delay. If the integration time was greater than the readout time, no delay should be observed, because the storage area would be completely read out before the next image would be transferred from the imaging area. Since the delay was observed even when the integration time was greater than the delay (600 ms in Table 3), it was concluded that the chip was not operating as expected in frame-transfer mode. Therefore, to acquire data for a time T, the number of frames f which was needed was calculated by using $f = \frac{T}{t + 480}$ where t was the integration time in ms.

Integration time (ms)	Number of frames	Expected acquisition time (ms)	Observed acquisition time (ms)	Delay per frame (ms)
30	100	3000	49400	464
250	20	5000	15100	505
600	20	12000	21570	478
0	20	0	9510	476
			Average Delay	**481**

Table 3 Summary of data used to estimate the delay between frames acquired with the CCD camera.

3.1.2.3 CCD camera: bias frames

A bias frame is a dark exposure taken with zero integration time. Examination of such a frame can give important information about the condition of a CCD chip. An ideal bias frame is a flat noise image in which the noise amplitude in the image is equal to the readout noise of the CCD in greylevels [Ab95]. The magnitude of variation of any

patterns which are identified in a bias frame should be compared to the magnitude of the readout noise to determine their significance. The tests of the bias frames follow the tests outlined by Abbott [Ab95].

Nine bias images were acquired with the camera in complete darkness. This data set was acquired twice, on different days. They were first visually examined to determine if there was any obvious unwanted structure. Some showed rectangular regions which had, on average, one higher greylevel than the surrounding regions. The source of this was never identified and these regions could have contributed to some of the variation in greylevels which was observed.

Abbott [Ab95] describes several types of noise to look for in a bias frame: electronic interference (wavy patterns), burst noise (several pixels in a row with significantly greater noise), salt-and-pepper noise (neighbouring pairs of high and low pixels), "hot" regions (regions which are brighter than the rest of the frame), or dark spots (regions which are dimmer than the rest of the frame). None of these were discovered in the bias frames.

The mean and standard deviation of the greylevel in a $1cm^2$ ROI in the centre of each frame was calculated. The mean values were within one greylevel of each other for all the frames. However, the second set of data had a lower mean value than the first set. The two sets were taken under the same conditions, with one exception: an extension to the cable which connects the camera to the computer was used when acquiring the second set of data. This second cable was necessary for any beam-on measurements due to the distance from the door to the accelerator in the treatment room. The second cable appears to have caused the mean value in the bias frames to drop from 24 greylevels to

19 greylevels. Therefore, for the remaining measurements, both cables were used to ensure consistency.

A median bias frame was constructed by assigning each pixel the median value of the corresponding pixels from the nine bias frames. Using the median frame, profiles were constructed by averaging 20 pixels around the centre line in both the horizontal and vertical directions. These are plotted in Figure 3-5. Also shown, for comparison, are plots of a profile one pixel wide in both directions. The gradient appeared to be approximately linear and increased from left to right and top to bottom across the bias frames. The individual bias frames showed a similar pattern. A linear fit was performed with the 20-pixel data and the slopes and intercepts of the lines are tabulated in Table 4.

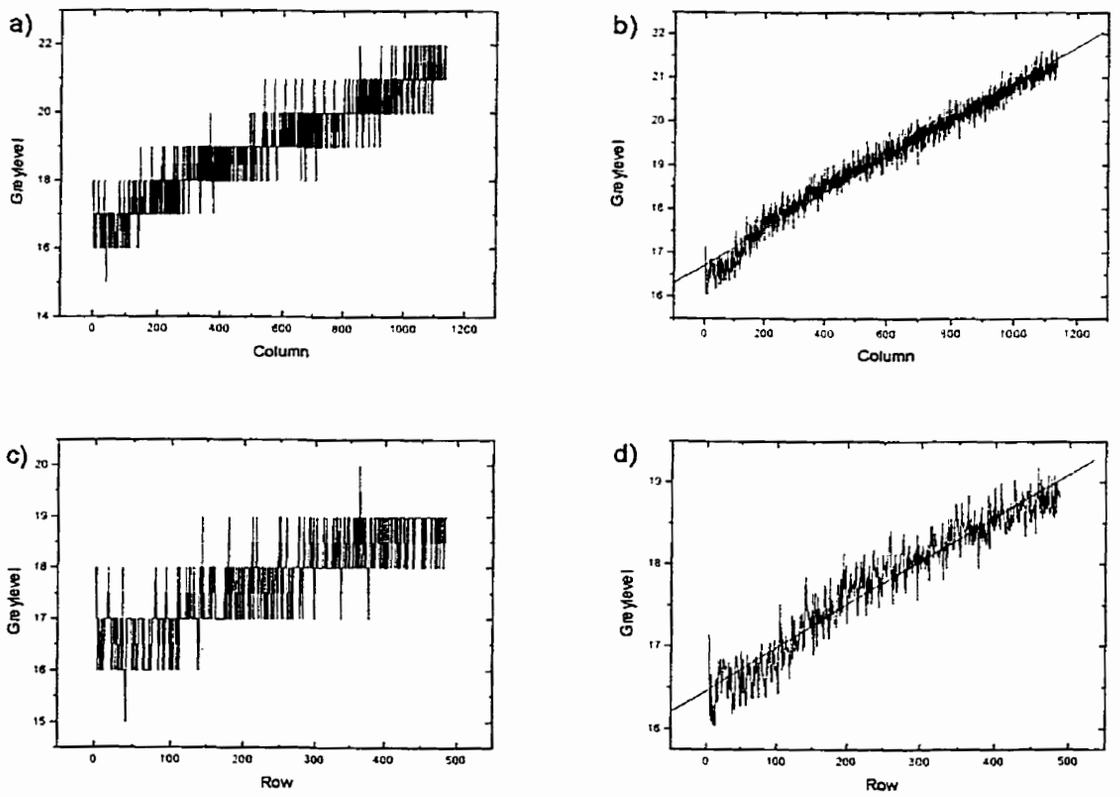

Figure 3-5 Plots of profiles of the median bias frame a) single line, horizontal direction; b) 20 pixels, horizontal direction; c) single line, vertical direction; d) 20 pixels averaged, vertical direction

Direction	Slope	Intercept	Correlation coefficient
Horizontal	0.00416 ± 0.00002	16.73 ± 0.01	0.98557
Vertical	0.00527 ± 0.00007	16.47 ± 0.02	0.95498

Table 4 Details of fitting for the slopes observed in the median bias frame.

The individual bias frames were analyzed in a similar manner to determine if the gradient was the same for each image. Table 5 shows the results of these fits, along with the mean values and standard deviations for the slopes and intercepts.

Direction	Bias frame number	Intercept	Slope
Horizontal	1	17.153	0.00417
	2	16.967	0.00419
	3	16.907	0.00417
	4	16.785	0.00412
	5	16.775	0.00418
	6	16.667	0.00418
	7	16.625	0.00417
	8	16.506	0.00419
	9	16.487	0.00409
	Mean	**16.763**	**0.00416**
	Standard deviation	**0.219**	**0.00003**
Vertical	1	19.5780	-1.55087e-006
	2	19.4037	8.53648e-005
	3	19.3577	0.000111252
	4	19.3016	-0.000124800
	5	19.3312	-0.000266767
	6	19.1395	-3.50488e-005
	7	19.0403	-4.01102e-005
	8	18.9089	-4.91285e-006
	9	18.8438	-6.25286e-005
	Mean	**19.217**	**-0.00004**
	Standard deviation	**0.244**	**0.00011**

Table 5 Summary of fitting parameters of all nine bias images, along with the mean and standard deviation in these values.

The parameters are substantially the same from frame to frame. Therefore, subtraction of background, which includes the bias frame effects, should be sufficient to remove the gradient introduced into the data by the bias frame.

A histogram of the greylevels in the entire image was constructed. These are shown in Figure 3-6 for both a single bias frame and the median frame. In both

histograms, the distribution appears normal, although slightly more heavily weighted toward the higher greylevels. An examination of the profiles in Figure 3-5 reveals that the variation across the bias frames is not exactly linear. For columns 0-200 and rows 0-100, the greylevels are actually somewhat lower than the fit line. This variation contributed to the slight skewing of the histograms.

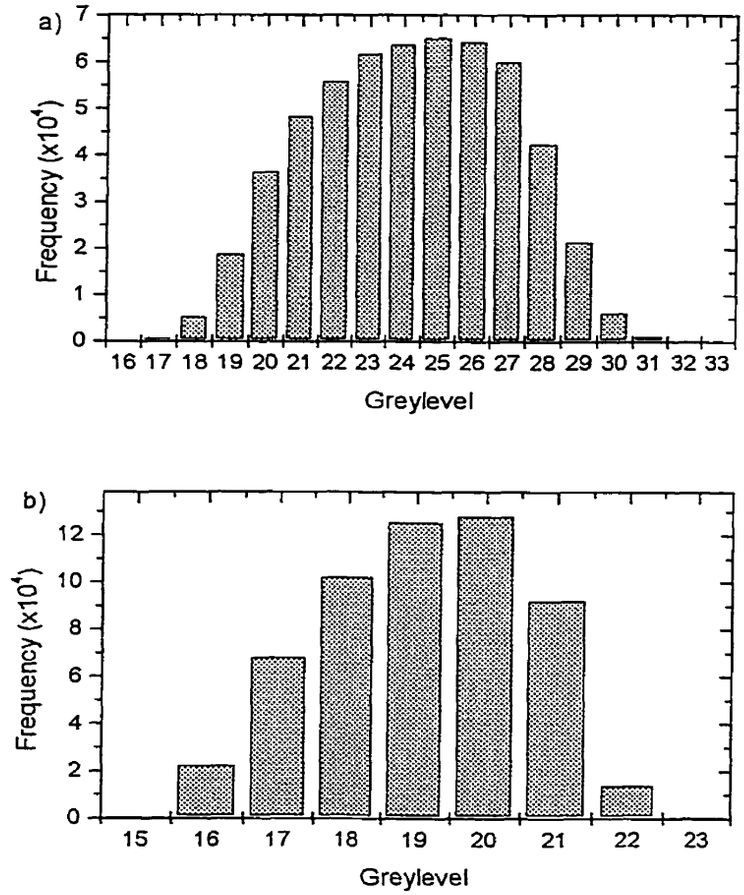

Figure 3-6 Histograms of the greylevels found in a bias frame for a) a single bias frame, and b) the median bias frame.

To attempt to quantify any noise signals, an analysis of the bias frames was performed using the Fast Fourier Transform (FFT). For each column, a linear fit was performed and subtracted from the data to remove the effects of the gradient in the bias level. The FFT was then performed on each column and the average over the entire image was calculated. The same procedure was repeated for the rows. The amplitude of the FFT of rows and columns is plotted in Figure 3-7 for both a single representative bias frame and the median bias frame.

No significant peaks were observed in the FFT of the columns, therefore, no significant interference was present in the vertical direction. The FFT of the rows did

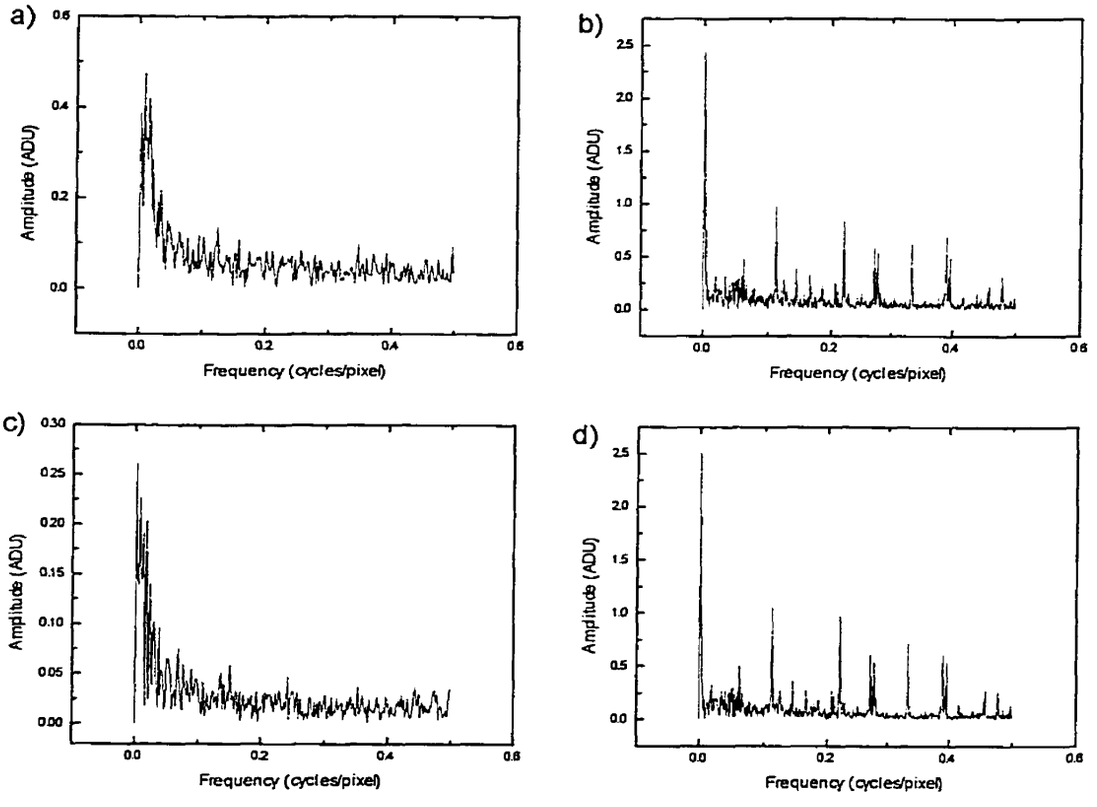

Figure 3-7 Plot of the mean FFT for a) the columns of a single bias image, and b) the rows of a single bias image, c) the columns of the median bias image, and d) the rows of the median bias image.

show some peaks on the order of 1.0 to 1.5 ADU for both the single bias frame and the median bias frame. Since the peaks were visible in a single frame as well as in the median frame, it can be concluded that they occur in every bias frame. This interference will therefore contribute to the readout noise of the CCD.

3.1.3 Noise and frames

The number of frames acquired is generally determined by the total time of data acquisition. However, for the experiments involving the light field, the number of frames used in the integration was not determined by the beam-on time, so an investigation was carried out to determine how the noise in the images changed with the number of frames collected.

The light-tight box was used for these measurements, along with a small light source on the ceiling and the plastic screen.

3.1.3.1 Newvicon camera

Since the number of frames cannot be precisely controlled by the user, but depends on the time for which the beam-on switch is active, the Newvicon camera was allowed to collect light field images for different lengths of time. The light level used, in the range of 10^{-7} W/cm^2, was comparable to that experienced in clinical measurements. The number of frames averaged ranged from 3 to 101, corresponding to approximately 3 s to 108 s of acquisition time. The mean greylevel and standard error were calculated in a 1cm^2 ROI in the centre of each image. The standard error was divided by the mean greylevel to give a measure of relative error in each ROI. Figure 3-8 shows a plot of these data as a function of number of frames acquired.

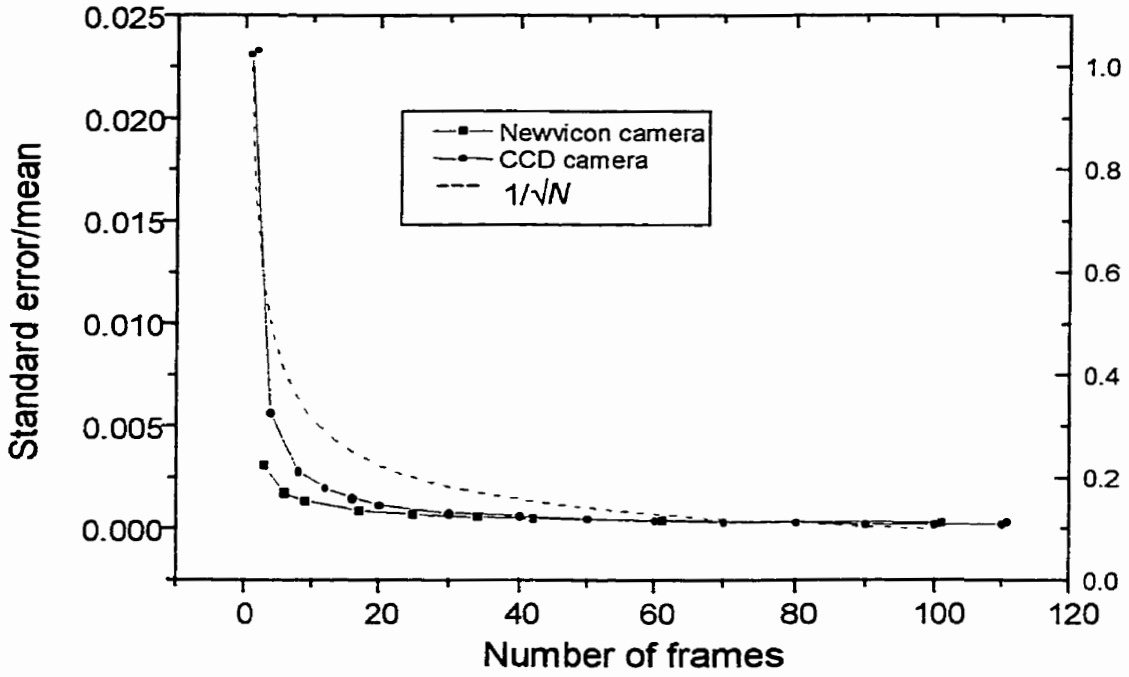

Figure 3-8 Plot of relative error as a function of number of frames acquired for the Newvicon camera (■) and the CCD camera (●). Included in the plot is the functional form expected for these data, $1/\sqrt{N}$, where N is the number of frames acquired. The right axis refers to the measured data, while the left axis refers to the function graph.

3.1.3.2 CCD camera

For the CCD camera, the number of frames acquired is directly controlled by the operator, so a number of different images were acquired with 30-ms integration times (similar to the frame rate of the Newvicon camera), each with different numbers of frames of varying from 1 to 110. This resulted in total imaging times from 0.5 s to 65 s. The mean greylevel and standard error were again calculated, and divided to give a measure of the relative error. Figure 3-8 shows a plot of these data.

3.1.4 Clamping

For any quantitative application, it is necessary to have good circuitry to clamp the video signal to a predetermined black level during the analog-to-digital (A/D) conversion [Ba80]. Clamping errors are manifested by the "video black" level being set at different levels for each video line depending on the degree of illumination on any given line and the size of the illuminated region [Raj95]. The quality of the camera and frame grabber board are important; poor clamping circuitry can result in errors as large as 5.5% [Raj95].

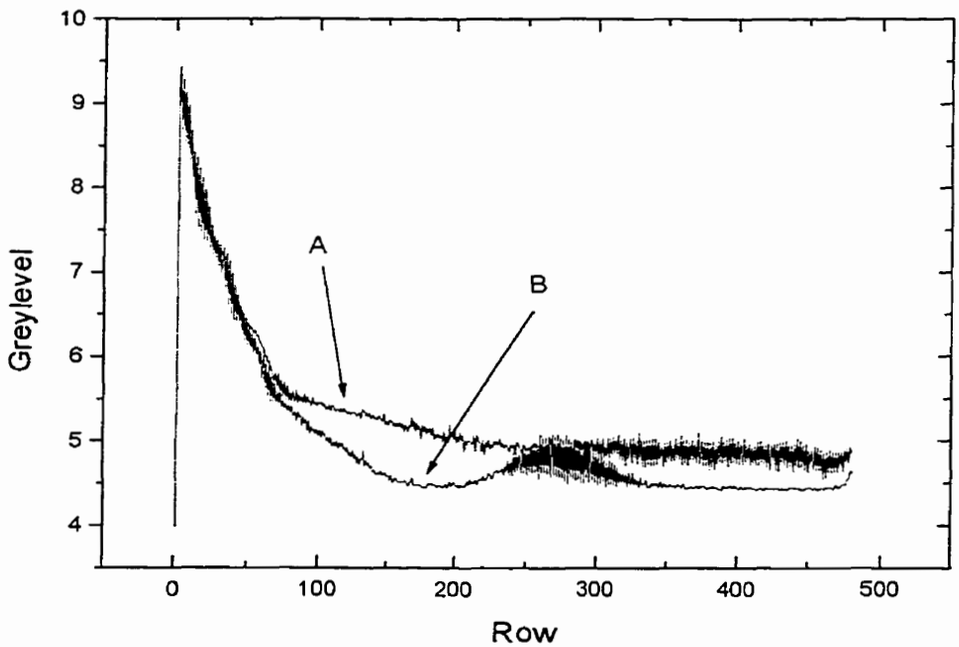

Figure 3-9 Vertical profiles, uncorrected for background, created by averaging 7 columns at the left-hand side of the usable image, for a 20-cm square light field (A) and a 5-cm square light field (B).

3.1.4.1 Newvicon camera

For the Newvicon camera, the first six columns of any image were always black and identically zero. These columns could not be considered to be part of the image, so the next few columns were analyzed for clamping error. To test the clamping circuitry, images were taken of several illuminated regions of different shapes (square and circular), sizes (5 cm and 20 cm diameter), and intensities, to determine if these variations had an effect on the black level. The different light intensities were achieved by using an extra piece of plastic between the light source and the screen, and the different shapes were made using cardboard collimators. The sizes of the collimators were such that there was a region on the left hand side of each image that was black. In this particular analysis, the images were not corrected for background because the clamping circuitry reacts to the entire signal received from the camera, including what is considered to be background signal.

Profiles were constructed of a 7-pixel wide region (columns 7 to 13) bordering on the zero region at the left-hand side of the image. On the whole, these profiles were very noisy. See Figure 3-9 for two sample profiles.

3.1.4.2 CCD camera

As with the Newvicon camera, it was necessary to investigate any possible errors in the clamping circuitry for the CCD camera. Images were again acquired of small and large square and circular fields. The integration time was changed to achieve different "intensities". Images were acquired with light fields of different shapes (square and circular), sizes (5 cm and 20 cm diameter), and integration times (30 ms, 60 ms, and

90 ms integration time). Figure 3-10 shows a sample plot of one of the profiles. They were all similar in appearance. Any other profile would overlap this one so as to obscure the shape of both, so only one is displayed.

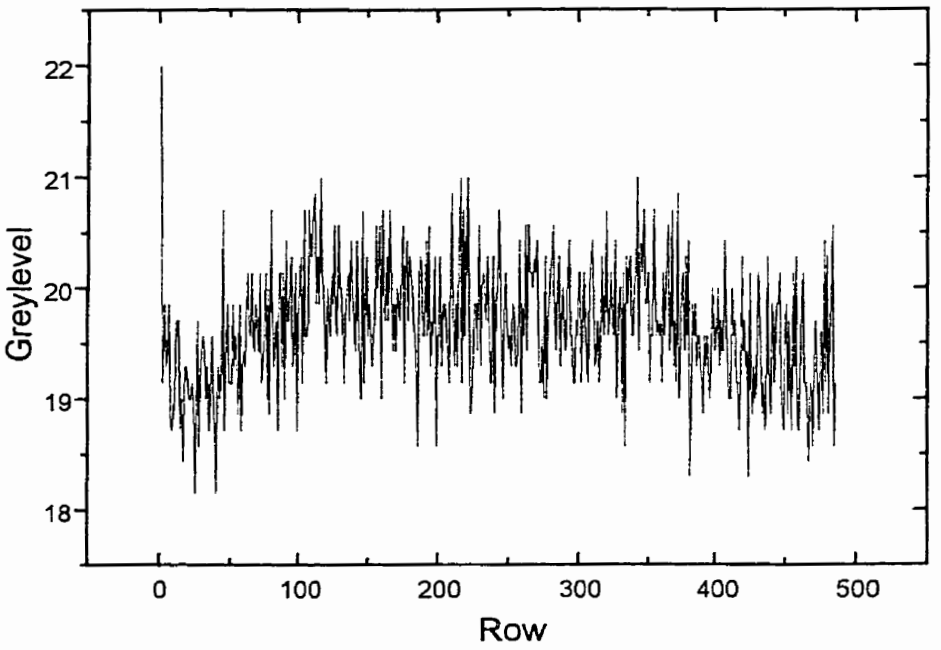

Figure 3-10 Vertical profile with the CCD camera, uncorrected for background, created by averaging 7 columns at the left-hand side of the image, for a 20-cm square light field with integration time of 90 ms.

3.1.5 Lens vignetting

3.1.5.1 Newvicon camera

To investigate the effects of lens vignetting, images were acquired of a flat light field at different aperture settings. Images were acquired with aperture settings ranging from F/1.1 to F/8.0. For the highest aperture stops (F/11.0 and F/16.0), the light field intensity observed by the camera was comparable to the background readings, so these

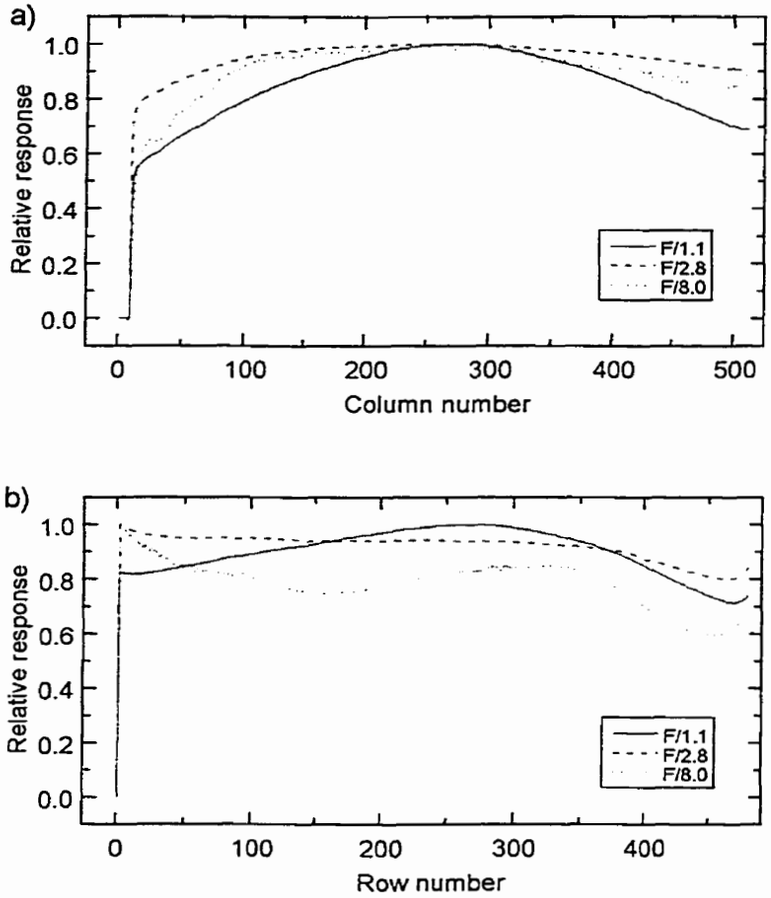

Figure 3-11 Plot of Newvicon camera profiles through a flat-field image in a) the horizontal, and b) the vertical direction, at aperture settings of F/1.1, F/2.8, and F/8.0.

measurements were not included. The images were background corrected and normalized to their maximum value. Plots of these profiles are shown in Figure 3-11 .

3.1.5.2 CCD camera

Images were acquired with the CCD camera using aperture settings from F/1.6 to F/8.0. These were analyzed in the same way as those for the Newvicon camera. Three representative profiles are plotted in both the horizontal and vertical directions in Figure 3-12.

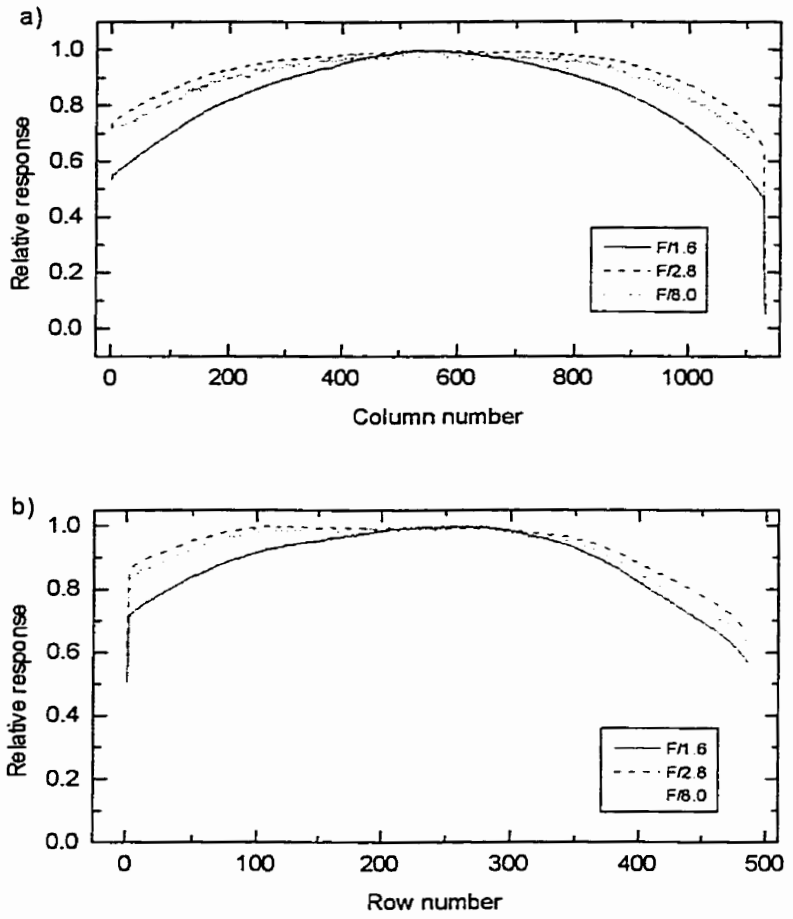

Figure 3-12 Plot of CCD camera profiles through a flat-field image in a) the horizontal and b) the vertical direction, at aperture settings of F/1.6, F/2.8, and F/8.0.

3.2 Spatial dependence of the EPID sensitivity

A series of measurements was carried out to test the spatial dependence of the EPID sensitivity. With the brass and phosphor screen in place, the EPID was irradiated with 100 MU of a 3 cm x 3 cm 6 MV photon beam at different locations on its entrance surface over a grid covering the central 21 cm x 33 cm of the field of view. To irradiate

the different grid points, the entire light-tight box was moved, so that the energy spectrum of the beam, and therefore the light source for the measurements, remained the same.

3.2.1 Raw data

The centre of each irradiated area was determined using the centre-finding software routine described in 2.6.4. The average greylevel and standard deviation in a 1 cm^2 area around the centre were calculated. The data were then interpolated to a grid of 40 x 40 points, covering the same area as the original grid, and plotted as a contour plot. Figure 3-13 shows these data for both the Newvicon camera (a) and the CCD camera (b).

3.2.2 Lens vignetting correction

To determine which part of the nonuniform response visible in Figure 3-13 was due to the light-tight box itself, the data were then corrected for the effects of lens vignetting. An "aperture correction image" was created using the image of the flat light field at the F/# used in this measurement. It was corrected for background and normalized to the value at the centre of the image. The image was then smoothed so as not to introduce excessive noise into the measurements.

The smoothed image was used to correct the EPID response at each location by dividing the observed greylevel in a given pixel by the aperture correction image value for that pixel. These data were again interpolated over a 40 x 40 grid to give a smoother image. Figure 3-14 shows the resulting contour plots. All other images acquired and analyzed in this report were corrected for the aperture setting after background subtraction by division of the acquired image by the aperture correction image.

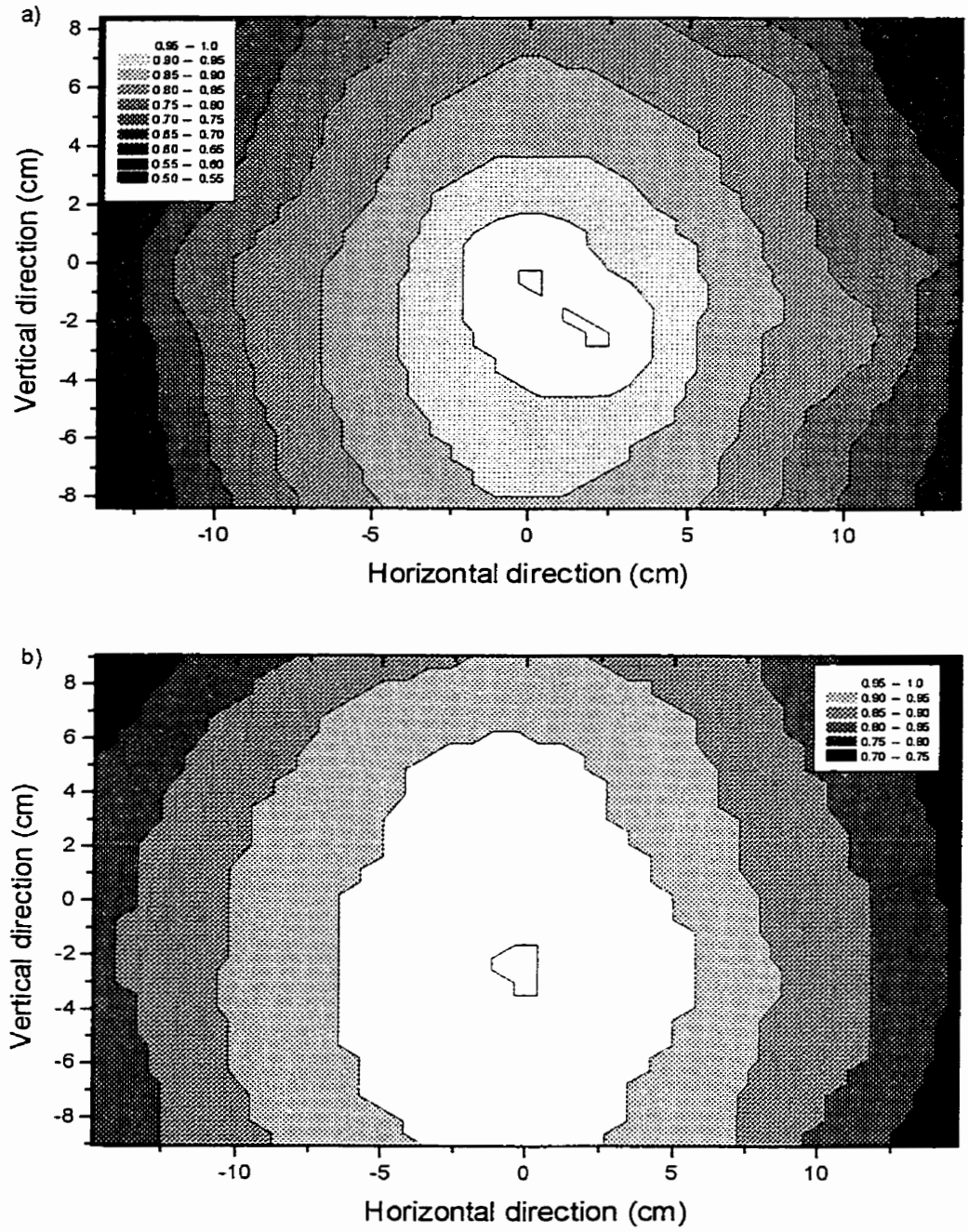

Figure 3-13 Contour plot of the raw sensitivity of the EPID system, for a) the Newvicon camera, and b) the CCD camera. The upper region of the plot corresponds to the part of the mirror nearest the phosphor screen.

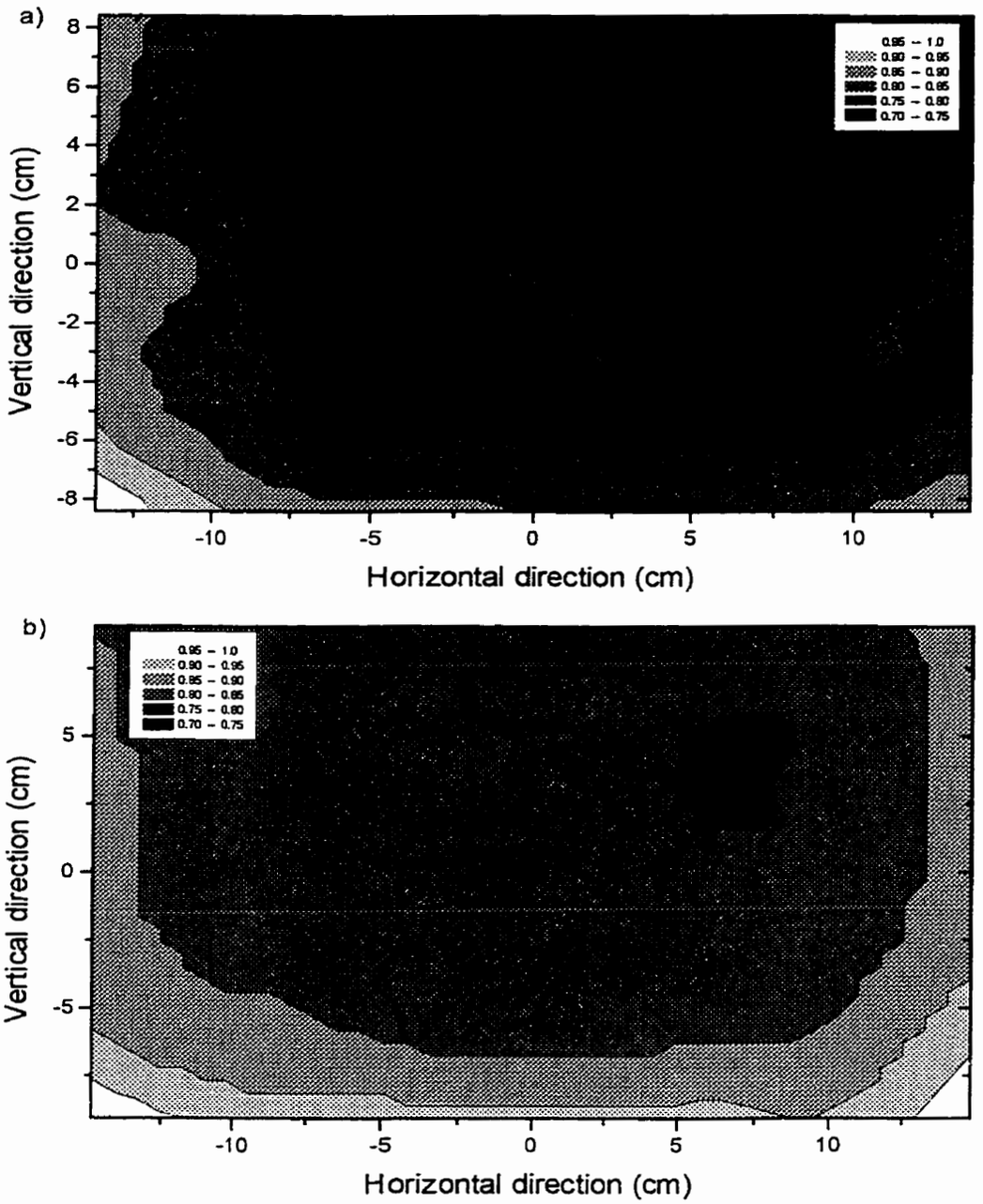

Figure 3-14 Contour plot of EPID sensitivity data with aperture correction applied for a) the Newvicon camera, and b) the CCD camera. The upper region of the plot corresponds to the part of the mirror closest to the phosphor screen.

3.3 Veiling glare

In an optical system, light which travels along paths not intended by the optical designer and appears in the image plane is referred to as glare. Glare can be observed in various forms: it can appear spread over the whole image, or it may be concentrated in patches [Ma81]. *Veiling glare* has been adopted as a term to describe this increase in light. Although the name implies a uniform "veil" of light over the whole image, its behaviour can in fact be much more complex. The main causes of glare are unwanted reflections and scatter [Ma81]. Any optical component can be involved in the production of glare, including optical surfaces, iris blades, edges of optical components, and mirrors [Ma81].

The veiling glare effect for the optical system which makes up the EPID was measured for a specific set of circumstances. Measurements were made of the change in greylevel observed at the central axis when the size of the illuminated region was varied.

3.3.1 Experiment A: whole system

To examine the veiling glare effect for the entire system as it would be used in a clinical situation, different sizes of square fields were used to irradiate the detector surface of light-tight box, and images were acquired of these irradiations. The field sizes used ranged from 2 cm x 2 cm to 27.7 cm x 27.7 cm at the EPID surface (1.4 cm x 1.4 cm to 20 cm x 20 cm at isocentre). The fields were centred in the field of view, and the dose administered was 100 MU. An ionization chamber was then set up as described in Section 2.6.4, and measurements were taken for the same set of field sizes and monitor units.

After background and vignetting corrections, the mean greylevel and standard error in the central 1 cm^2 of the squares was calculated, divided by the ionization chamber reading to account for changes in head scatter, and plotted as a function of irradiated area. Figure 3-15 shows a plot of both the raw data and the data divided by ionization chamber readings for the Newvicon camera (a) and the CCD camera (b).

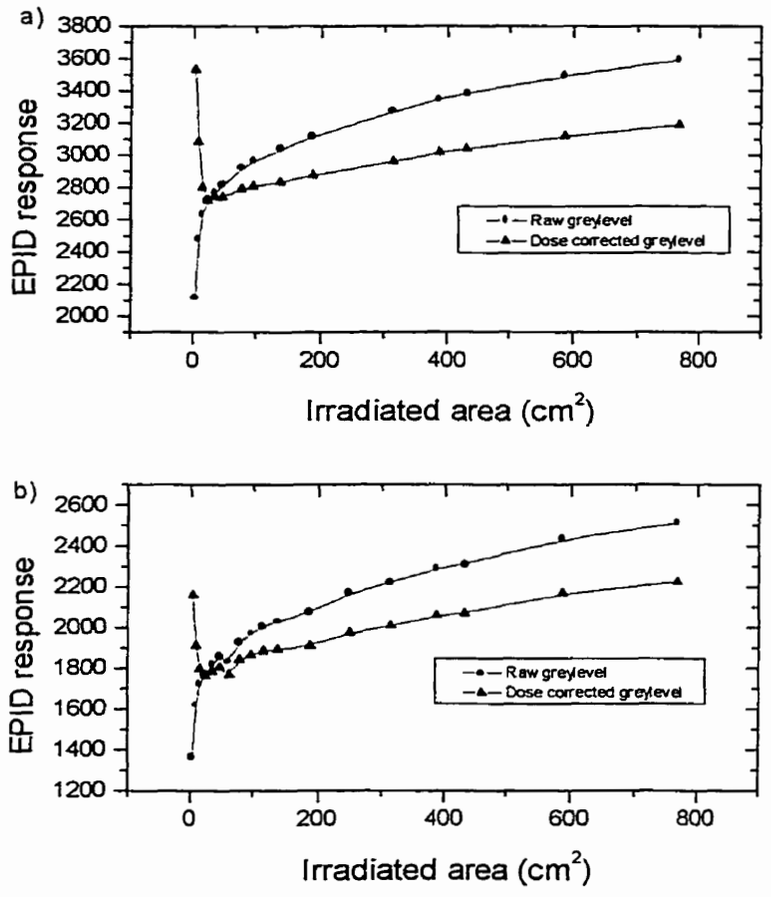

Figure 3-15 Plot of the EPID response as a function of irradiated area for a) the Newvicon camera, and b) the CCD camera. The circles indicate the raw greylevel, while the triangles indicate the greylevel divided by the ionization chamber reading. The error bars are too small to be seen on this scale.

3.3.2 Experiment B: light source, with mirror

To determine the degree of glare caused by the radiation and the brass/phosphor screen combination, experiment A was repeated using a visible light source instead of a radiation field. A light source on the ceiling, as described in Section 2.2, provided a uniform field at the surface of the detector.

Circular and square black cardboard collimators were used to define light fields at the surface of the detector. The detector surface consisted of the phosphor screen attached to a frame which was mounted in the opening of the light-tight box. The phosphor screen was translucent. When it was illuminated from outside the light tight box with a light source at the ceiling, the light field was uniform within ± 2% as measured by a radiometer over the 20 cm x 20 cm square region being studied. The concentric collimators were centred in the field of view of the cameras. Their sizes ranged from 2 cm diameter to 20 cm diameter for the circles, and 2 cm to 20 cm length of side for the squares, all defined at the EPID surface. The different shapes were used to determine if the glare depended on shape as well as illuminated area.

The light source was not particularly stable, so light intensity measurements using a radiometer were interspersed with the image acquisition. A linear regression was performed with the light intensity measurements, and the data from the fit were used in correcting the greylevel data for the change in light level. The plot of these data and the results of the fitting are shown in Figure 3-16.

The camera responses in this range of light levels was known to be linear. To use the derived corrections, the fitted values were normalized to the highest value in each series to give a correction factor for each measurement. The data were then corrected by

dividing each measured greylevel by its correction factor. Using standard rules for the propagation of error, combined with the uncertainties in the fitted parameters, indicated that the errors introduced by this procedure range from 0.25% to 0.76%, with a mean uncertainty of 0.44%.

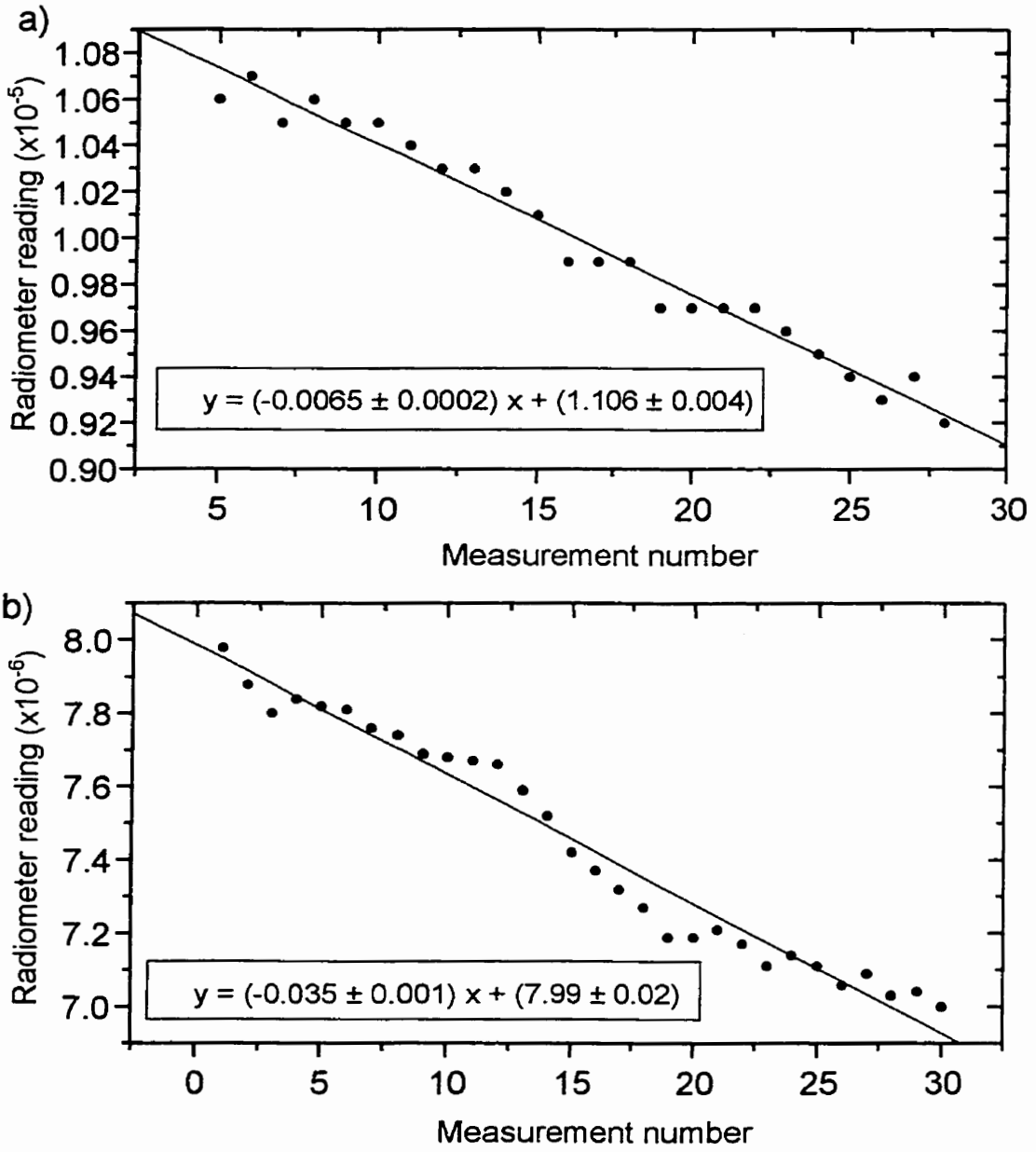

Figure 3-16 Plot of data and linear fits performed to correct for the decreasing light intensity in experiment B for a) the Newvicon camera, and b) the CCD camera.

After background subtraction and lens vignetting correction, the mean greylevel and standard error in a 1 cm^2 ROI in the centre of the squares (or circles) was calculated and plotted as a function of illuminated area. These plots are shown in Figure 3-17.

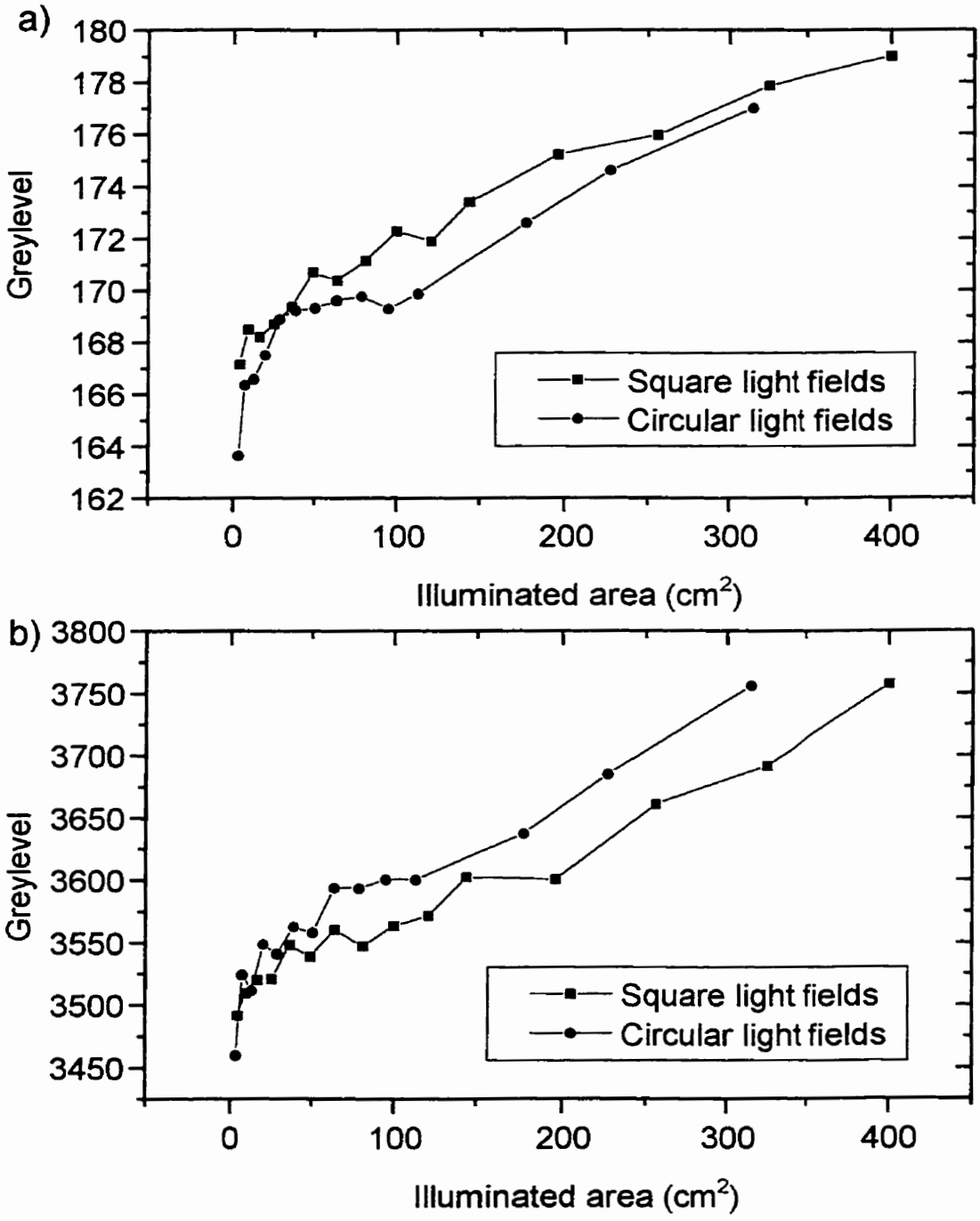

Figure 3-17 Plot of the EPID response in the centre of the image as a function of illuminated area, with a visible light source, for a) the Newvicon camera, and b) the CCD camera. The error bars are too small to be seen on this scale.

3.3.3 Experiment C: light source, no mirror

To isolate camera effects, the veiling glare experiment was repeated one more time with no mirror present. The light box described in Section 2.3 was used for this experiment along with the cardboard collimators used in experiment B.

The intensity of light from the light box varied with field size. The change was caused by the fact that the black paper used to construct the collimators was not perfectly absorbing, so that as the field size decreased, the amount of light reflected back into the box and then escaping through the remaining opening increased. The light field measurements were recorded for each field size and used to correct the measured greylevels as described in the previous section.

After background and vignetting correction, the mean greylevel and standard error were calculated in a $1cm^2$ ROI at the centre of each image, corrected for light intensity variations, and plotted as a function of illuminated area in Figure 3-18.

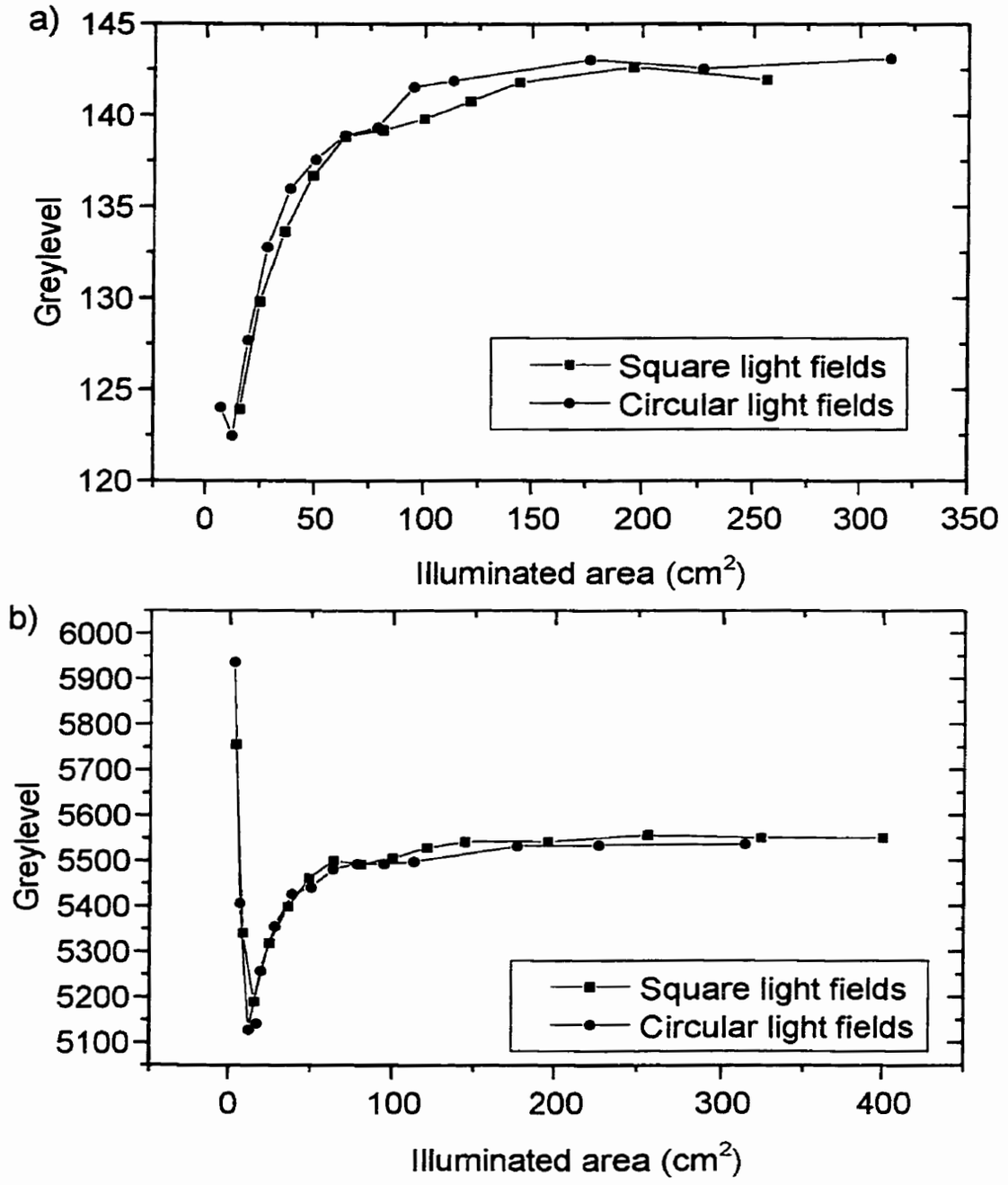

Figure 3-18 Plot of EPID response at the centre of each image as a function of illuminated area, without the mirror present in the optical chain, for a) the Newvicon camera and b) the CCD camera. Note that the error bars are too small to be seen on this scale.

3.4 Dosimetry

Preliminary investigations were carried out to characterize the EPID response with dose.

3.4.1 Linearity with monitor units

To test the linearity of the EPID response with increasing numbers of monitor units, a phantom was irradiated with doses in the range of values used clinically, and the EPID response was measured.

The phantom consisted of 18 sheets of acrylic, 40 cm x 40 cm x 1.11 cm. The water-equivalent thickness of phantom used in these measurements was 23.9 cm. The phantom was placed so that its exit surface was at a distance of 30 cm from the EPID. A 13.8 cm x 13.8 cm field at the EPID surface (10 cm x 10 cm at isocentre) was used to irradiate the phantom and EPID with monitor units from 25 to 300 MU, in steps of 25 MU. A plot of this data is shown in Figure 3-19. The data were fit to a straight line, with parameters as outlined in Table 6.

There appeared to be one bad data point for each plot: 200 MU for the Newvicon camera, and 100 MU for the CCD camera. Assuming a Gaussian error distribtuion, the probability that these points were representative of the data was 2.3% for the Newvicon 200 MU point and 0.4% for the CCD 100 MU point. Since these probabilities were small, the fits were repeated excluding these points, and the parameters are shown in Table 6.

The bad data point for the Newvicon camera at 200 MU was later determined to have been caused by the camera not acquiring the proper number of frames. For 200 MU, the acquisition should have consisted of 40 frames, but examination of the header file showed that only 38 frames were acquired. The cause of the bad data point at 100 MU for the CCD camera was not found.

Camera	Points included	Slope	Intercept	χ^2_ν
Newvicon	all	11.30 ± 0.05	7 ± 5	1140
	all except 200 MU	11.33 ± 0.04	6 ± 4	645
CCD	all	7.24 ± 0.07	16 ± 9	686
	all except 100 MU	7.24 ± 0.01	11 ± 2	28.49

Table 6 Summary of parameters from the fits shown in Figure 3-19.

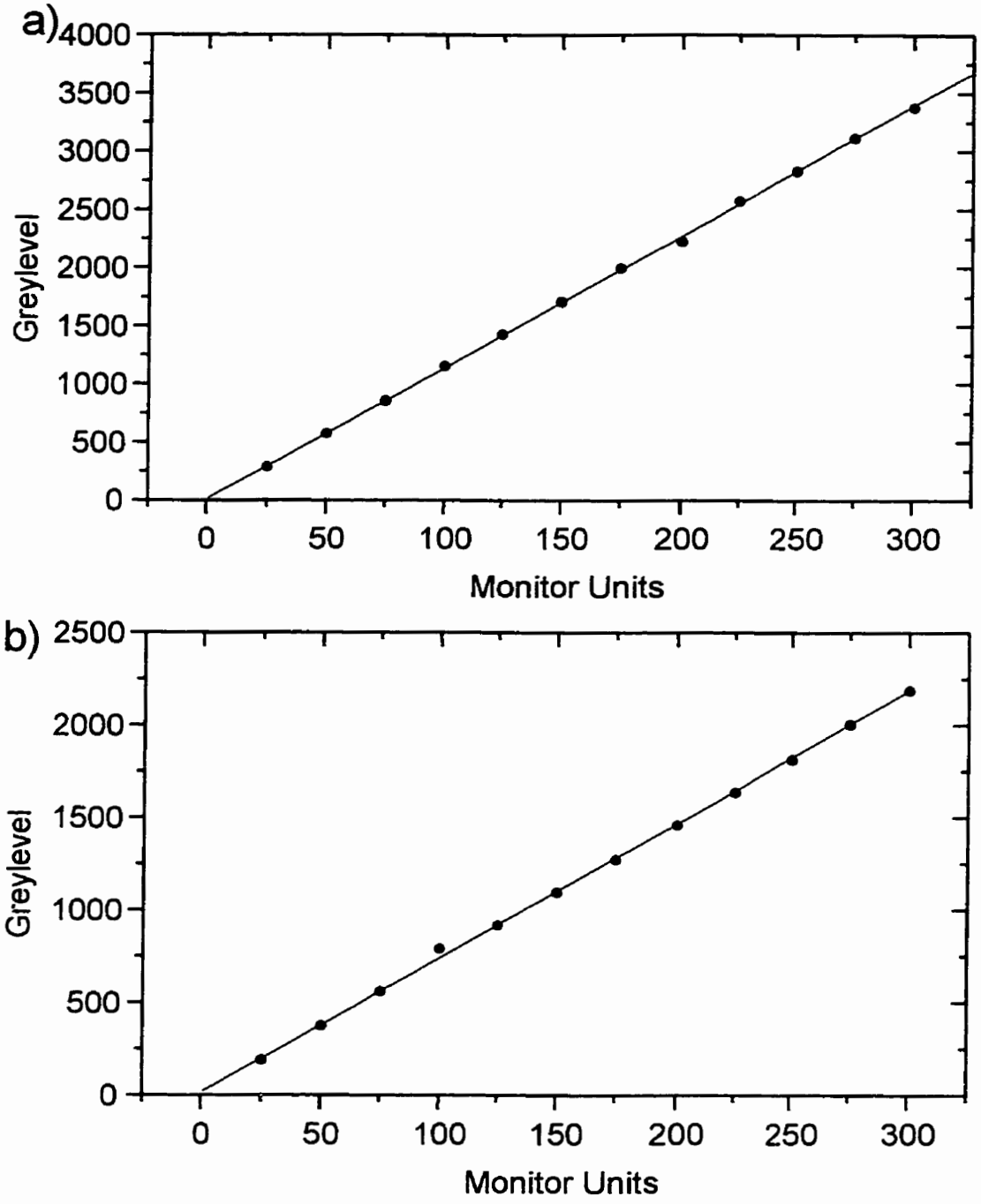

Figure 3-19 Plot of EPID response as a function of monitor units for a phantom thickness of 23.9 cm and a field size of 10 cm x 10 cm for a) the Newvicon camera and b) the CCD camera. Note that the error bars are too small to be seen on this scale.

3.4.2 Response with absorber thickness, field size

Measurements were made to determine the response of the EPID to changes in absorber thickness and field size. The acrylic phantom described in the previous section was placed in the beam with thicknesses of phantom ranging from 0 to 18 pieces of acrylic, in steps of 3. The exit surface to EPID distance was kept constant at 30 cm for all the measurements. Square fields of side 6.9 cm, 13.8 cm, 20.7 cm, and 27.7 cm at the EPID surface (5 cm, 10 cm, 15 cm, 20 cm at isocentre) were used, and a dose of 100 MU was delivered. For the Newvicon camera, 20 frames were used to acquire the data, while for the CCD camera, 40 frames of 250 ms each were used to acquire the data. The mean and standard error in a 1 cm^2 ROI at the centre of each field were calculated for each image. The data are plotted in Figure 3-20.

Ionization chamber measurements were also taken under identical conditions, as described in Section 2.6.5. Figure 3-21 shows plots of the greylevels divided by the ionization chamber readings for both cameras.

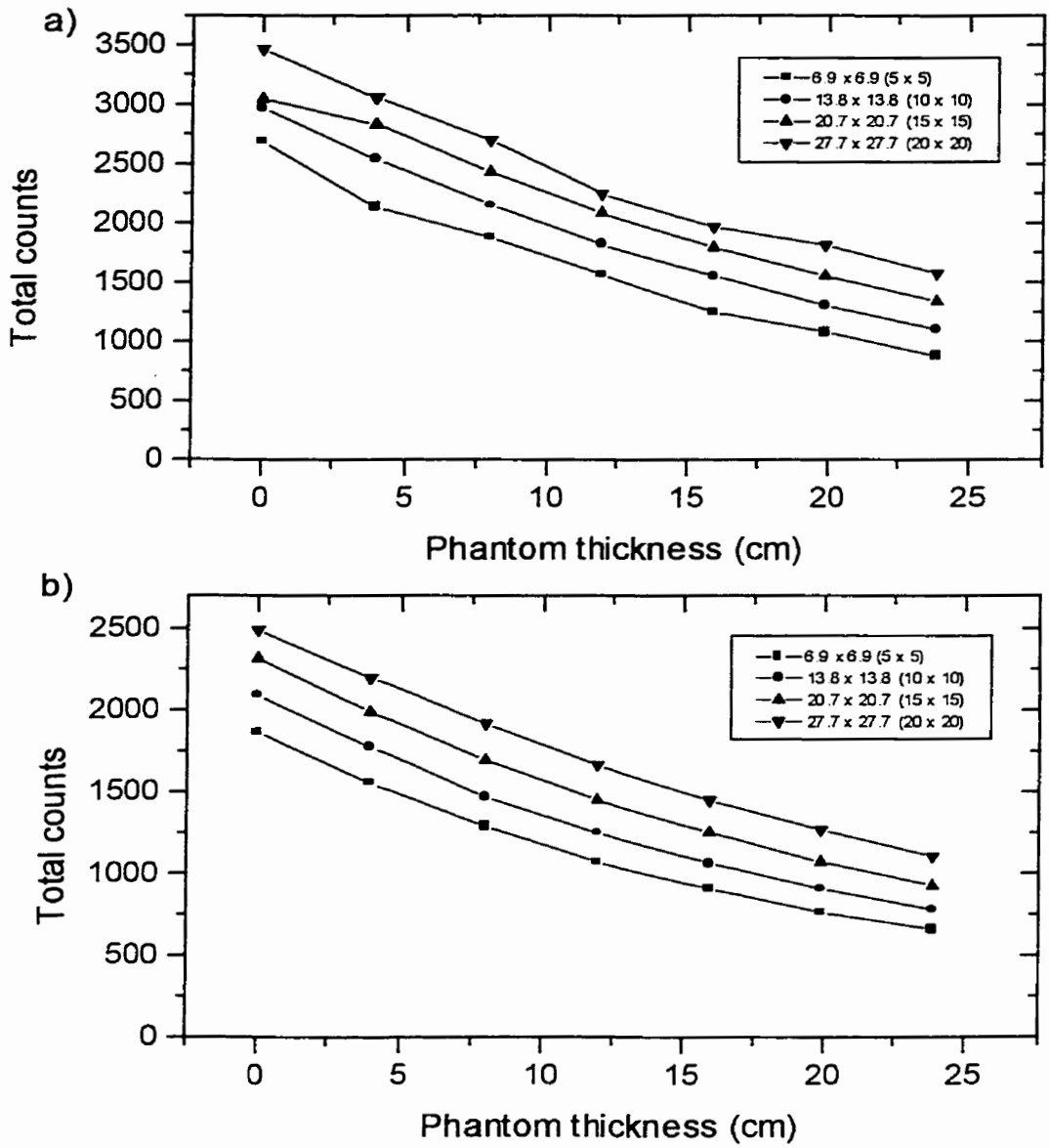

Figure 3-20 Plots of change in total counts with field size and absorber thickness for 100 MU delivered for a) the Newvicon camera, and b) the CCD camera, for field sizes at isocentre of 5 cm x 5 cm (ν), 10 cm x 10 cm (λ), 15 cm x 15 cm (σ), and 20 cm x 20 cm (τ). Note that the error bars are not shown as they are similar in size to the plotted points themselves.

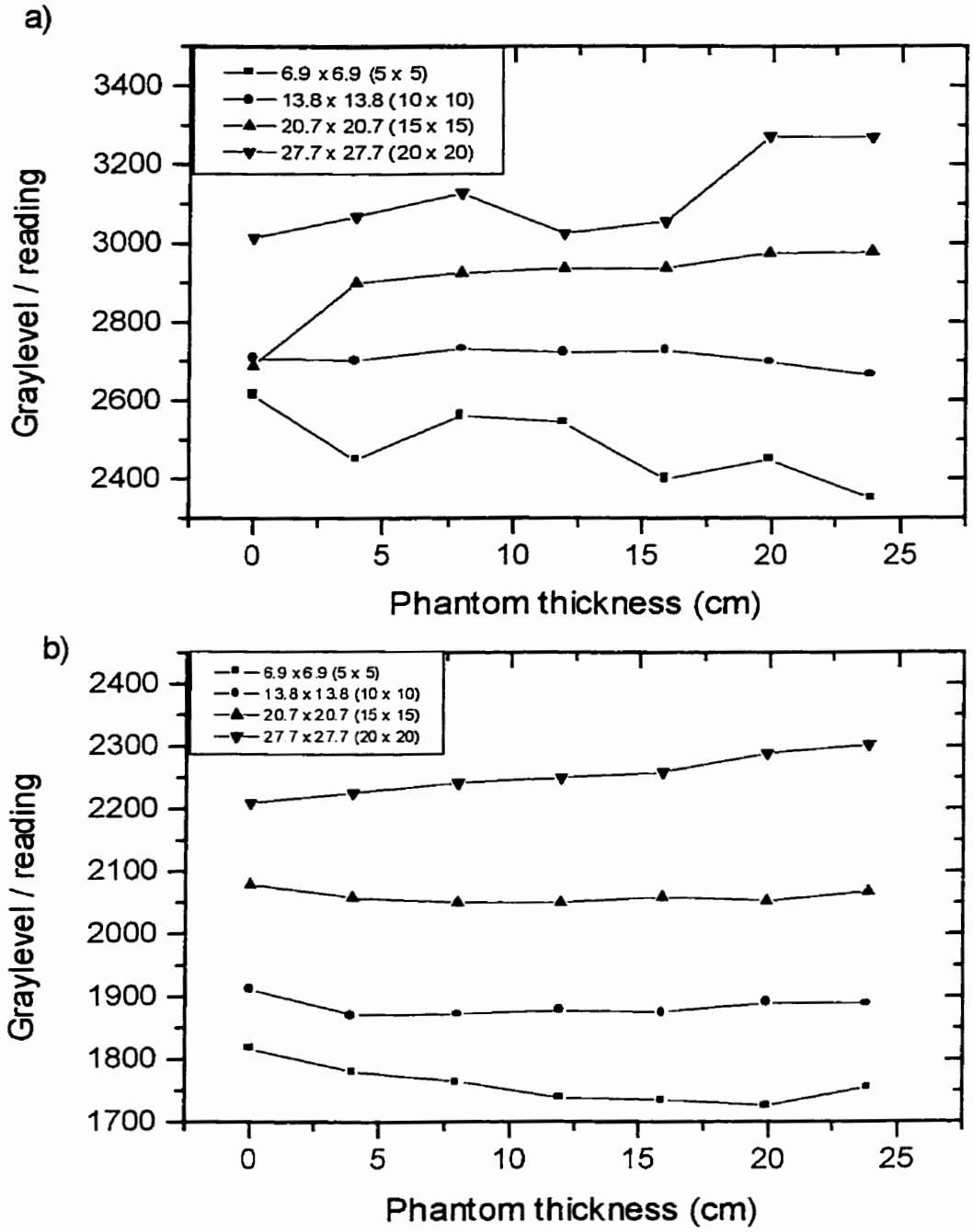

Figure 3-21 Plot of measured greylevel divided by ionization chamber reading for different field sizes and phantom thicknesses for a) the Newvicon camera, and b) the CCD camera, for field sizes at isocentre of 5 cm x 5 cm (ν), 10 cm x 10 cm (λ), 15 cm x 15 cm (σ), and 20 cm x 20 cm (τ). Note that the errors are too small to be seen on this scale.

4 Discussion

4.1 Camera tests

4.1.1 Linearity

Table 2 showed the parameters for the linear fits for both cameras.

For the Newvicon camera, the value for χ_v^2 is extremely high. A good fit with uncertainties which accurately account for the spread in the data should produce a value of unity for χ_v^2. The high value for χ_v^2 is probably due to the underestimation of the uncertainty in the data. The error bars used in the analysis of Figure 3-1 were the standard error of the greylevel values in the central 1 cm^2 ROI. Therefore, there is greater variation in the greylevel values recorded by the Newvicon camera than is accounted for by their standard error alone.

The intercept from the Newvicon data fit is negative. It would be expected, as a first approximation, to equal zero within its uncertainty; however, it does not. A sigmoidal response is typical of a video tube. It is probable that at lower light levels, beyond those investigated here, the camera's response is no longer linear, but instead "flattens off" as it approaches zero. This could result in the fitted intercept being negative.

The fit for the CCD camera is better than the fit for the Newvicon camera, in terms of the χ_v^2. However, the χ_v^2 is still too high, and again indicates that there is more variation in the data than can be accounted for by the standard error. The intercept from the CCD data is not zero, but instead shows the bias level for this CCD camera.

4.1.2 Noise and frames

Figure 3-8 showed a plot of the relative error (standard error in an ROI divided by the mean greylevel in the ROI) as a function of numbers of frames acquired. Preliminary light field data with the Newvicon camera resulted in very noisy data. Those measurements, not shown here, had been made with only 11 or 12 frames each. After analysis of Figure 3-8 it became evident that at least some of the noise observed was due to the low number of frames acquired. In fact, the error decreases as the number of frames increases up to about 40 frames, and levels off after that. Therefore, all Newvicon light field data displayed in this report were acquired with at least 40 frames, to reduce this source of noise.

For the CCD camera, a single frame has a larger relative error than the Newvicon camera. Figure 3-8 shows this variation to be almost 2.5%. This drops rapidly with an increasing number of frames, and is less than 0.5% for 30 frames or more. To reduce this source of noise, all light field data with CCD camera were acquired with 40 frames. It should be recalled that the Newvicon camera "frame" is actually a 32-frame average already, before it is summed in the frame buffer, so it is not surprising that the relative error is smaller for the Newvicon camera.

The expected functional form of the relationship between error and number of frames is presented in Figure 3-8 as a dashed curve. When averaging N values, the error in the mean is proportional to $1/\sqrt{N}$. However, the data shown do not show the expected form. Instead of continuing to decrease indefinitely as the number of frames increases, the relative error levels off after about 40 frames. Therefore, some of the variation observed in the measured data points is fixed and does not decrease with the number of

frames averaged. This additional noise, which contributes to the observed standard error, may be from a number of sources. The interference effects noticed in the bias frames could contribute to the standard error, as well as electronic noise from the camera and its associated circuits.

For 100 MU of radiation, the Newvicon camera acquired 20 frames while the CCD camera acquired 40 frames. Both these numbers fall on the plateau region of the curve in Figure 3-8. More error in the measured greylevels will be introduced by the interaction of the radiation with the brass and phosphor, but the error stemming from the light collection part of the system will be reduced through the frame averaging process.

4.1.2.1 Problem with Newvicon acquisition program

The software used to acquire the data with the Newvicon camera did not always behave as expected. A "beam-on" input to the computer from the accelerator normally indicates to the software that data acquisition should begin. When the beam-on signal terminates, the software should acquire one additional frame, to account for any afterglow in the phosphor, and then stop. The output of the accelerator is very stable; a 100-MU irradiation involves 0.33-0.34 minutes of beam-on time.

The number of frames acquired, as recorded in the header files, occasionally varied from the 20 frames expected for this beam-on time. Some of the 100 MU radiation field images were acquired with 18 or 19 frames, instead of 20 frames. Variations in machine output were not large enough to account for such a change. If the header files are to be believed, then the acquisition was terminated early for some images. The reason why this happened was never discovered.

Figure 4-1 shows two plots based on the ionization chamber-corrected field size and phantom thickness data shown already in Figure 3-21 (a). Figure 4-1 (a) is the data from Figure 3-21 (a); Figure 4-1(b) is the same data divided by the numbers of frames recorded in the header file. (The 13.8 x 13.8 cm field was not included in this plot, because by sheer luck all of the data points for that field size were acquired with the correct number of frames.)

For the circled points in Figure 4-1, only 18 frames were acquired instead of the anticipated 20 frames; for the other points, 20 frames were acquired. The circled points do not lie anywhere near a smooth line in either Figure 4-1 (a) or Figure 4-1 (b). They lie below the lines in Figure 4-1 (a) and above the lines in Figure 4-1 (b). If the camera had failed to acquire an entire frame, dividing by the number of frames should have rectified the problem. However, from Figure 4-1 (b) it can be seen that the greylevel per frame is higher than anticipated. Therefore, the camera must have acquired more than 18 frames for those points, but not a full 19 frames, and recorded only 18 frames in the header file.

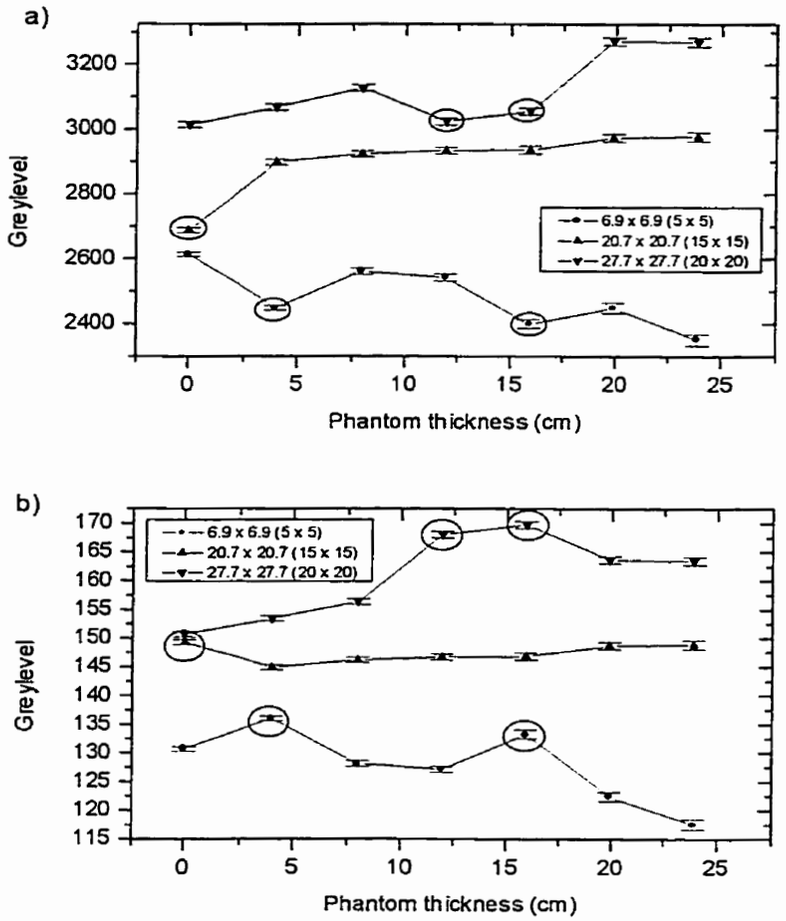

Figure 4-1 Plots demonstrating the errors in data points (circled) caused by lost frames when plotting a) total greylevel, and b) greylevel per frame.

4.1.3 Clamping

4.1.3.1 Newvicon camera

There appeared to be some differences in the profiles used to analyze the clamping error, in spite of the noise (see Figure 3-9). The differences, although very small, depended on the size and intensity of the illuminated region. Examining the mean value of the greylevel in those first few columns for each image made it easier to quantify

the differences in spite of the large amounts of noise. Table 7 shows the mean and standard error in the greylevels in these columns.

Small light fields tended to have their black level clamped to a lower number than larger light fields. Furthermore, the black levels did not agree with each other within the limits allowed by their uncertainties. However, the difference between the highest and lowest value was 0.42 greylevels, which was 0.2% of the 255 maximum greylevels possible in the image. Therefore, the errors in clamping were deemed negligible.

Shape	Diameter	Light level	Mean greylevel ± SE
Square	5 cm	Low	4.98 ± 0.04
Square	20 cm	Low	5.31 ± 0.04
Square	5 cm	High	4.89 ± 0.04
Square	20 cm	High	5.07 ± 0.04
Circle	5 cm	Low	4.92 ± 0.04
Circle	20 cm	Low	5.01 ± 0.04
Circle	5 cm	High	4.90 ± 0.04
Circle	20 cm	High	5.05 ± 0.04

Table 7 Details of images acquired to investigate clamping error in the Newvicon camera

4.1.3.2 CCD camera

The analysis of the CCD camera clamping data, which was just as noisy as the Newvicon camera data, was treated in the same way as that for the Newvicon camera. The mean and standard error in the greylevel values were calculated for each type of profile. Table 8 shows a summary of the data acquired.

In most cases, the images with a smaller illuminated region showed a lower average black value. However, the differences were still very small. The difference between the lowest and highest greylevels is 1.89 greylevels, or 0.7% of the maximum of 255 greylevels available. Therefore, the clamping error was considered to be negligible in comparison to other sources of uncertainty of the CCD.

Shape	Diameter	Integration Time	Mean greylevel ● SE
Square	5 cm	30 ms	19.71 ± 0.02
Square	20 cm	30 ms	19.98 ± 0.02
Square	5 cm	60 ms	20.03 ± 0.02
Square	20 cm	60 ms	20.49 ± 0.02
Square	5 cm	90 ms	20.11 ± 0.02
Square	20 cm	90 ms	19.65 ± 0.03
Circle	5 cm	30 ms	19.15 ● 0.02
Circle	20 cm	30 ms	19.96 ± 0.02
Circle	5 cm	60 ms	19.49 ± 0.02
Circle	20 cm	60 ms	20.49 ± 0.02
Circle	5 cm	90 ms	19.70 ± 0.02
Circle	20 cm	90 ms	21.04 ± 0.03

Table 8 Details of images acquired to investigate clamping error in the CCD camera

4.1.4 Lens vignetting

In both cameras, the lens vignetting effect is most severe for the largest aperture opening. Unfortunately, due to the low light levels experienced in portal imaging, this is the aperture setting which must be used in data acquisition. In Figure 3-11 and Figure 3-12, the profiles chosen for plotting were selected because they represented the two extremes of aperture settings, as well as the aperture setting which resulted in the least variation across the field of view. For both the Newvicon and CCD cameras, the "ideal" aperture setting was F/2.8 for both cameras.

For the Newvicon camera, the vertical profiles took on a strange shape, indicating that something in addition to lens vignetting is causing an increased response toward the top of the image. The cause of this unexpected response was never identified.

4.2 Spatial dependence

4.2.1 Removal of lens vignetting effect

As described in Section 3.2.2, all images were corrected for lens vignetting by dividing the background corrected image by the aperture correction image. This served to remove the drastic effects caused by the use of the largest aperture available on the lenses.

4.2.2 Source of asymmetrical response

Even after correction for aperture effects, the system as a whole showed a nonuniform response in the vertical direction. From examination of Figure 3-17, it can be seen that the response of the system to a light input near the "bottom" of the image (where the mirror was farthest from the phosphor screen) was up to 25% greater than near the middle or top of the image. Subsequent measurements were made to attempt to determine the cause of this nonuniformity.

The camera was immediately excluded as a suspect because both cameras demonstrated the same effect. The radiation field used for all the different grid points was identical, because it was the box which was moved around, rather using than the asymmetric jaw settings on the linear accelerator. Therefore the radiation field could not have been the cause.

To determine if the effect was caused by the brass/phosphor screen, the brass/phosphor screen was rotated by 180°. The sensitivity measurements were repeated for the grid points around the edges of the region, where most of the variation was observed. In spite of this rearrangement, the higher greylevel for the same light input still

appeared near the bottom of the image, indicating quite clearly that this effect was not due to the brass or phosphor.

The increased response may be caused by the angle of the mirror. The mirror's presence in the optical chain can introduce scatter: because of roughness on the mirrors' surface, light reflected from the mirror may not be reflected at precisely the angle expected and subsequently be observed at the corresponding position on the detection surface of the camera, but it may be reflected at a slightly different angle. Over the distance between the mirror and the camera, a small angular deflection could cause a photon which originated in the ROI being investigated to deviate sufficiently that it would not be counted by the camera in the ROI. Instead, it would be counted somewhere outside of the ROI.

Furthermore, since the mirror is situated at a 45° angle to the optical path, the distance between the mirror and the camera is different for the bottom and the top of the 33 cm x 21 cm region studied. Therefore, the solid angle subtended by the ROI used in the average is larger for a point near the bottom of the mirror than near the top. In fact, the ratio of solid angle subtended at the bottom of the region studied to that at the top of the same region is 1.42 for the Newvicon camera and 1.37 for the CCD camera. If the mirror introduces a small amount of scatter into the photons, it is thus possible that more photons would succeed in being counted when they originate near the bottom of the mirror than the top of the mirror.

4.3 Veiling glare

4.3.1 CCD camera: "Electronic overshoot"

Both cameras showed a slight increase in greylevel with field size for very small field sizes when the light box was used. Rajapakshe [Ra93] also observed this effect and quoted Roehrig and Fu as having observed and explained this phenomenon as "electronic overshoot". The sharp gradient present at the edge of the light field causes electronic instability and overreaction in the camera. Figure 4-2 shows horizontal profiles constructed by averaging 12 pixels in some of the light field data. The "horns" characteristic of this effect are clearly visible. The light field itself was checked with a radiometer to ascertain that the horns were not real. The radiometer showed no such variation across the edge of the light field.

For small field sizes, the "horns" overlap and cause an apparent increase in greylevel. Therefore, the data for the small light field sizes do not represent veiling glare and should not be used. However, such sharp gradients are never present in radiation fields, because the penumbra is much wider. Figure 4-3 shows profiles through the images acquired using radiation fields. The horns are not present. The increase in response near the field edges is due to the imperfect flatness of the radiation field itself.

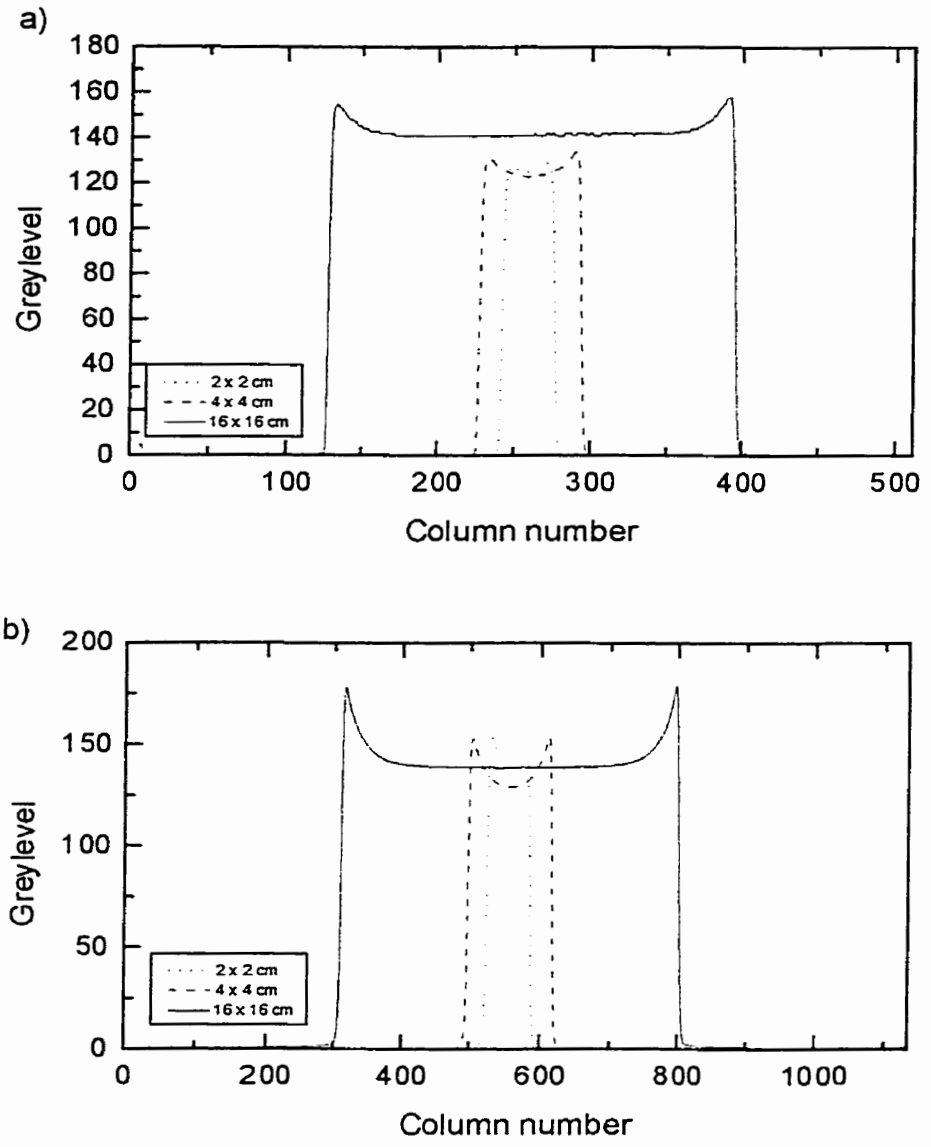

Figure 4-2 Profiles of images of light fields for a) the Newvicon camera, and b) the CCD camera, for square field sizes of 2 cm, 4 cm, and 16 cm at the detector surface.

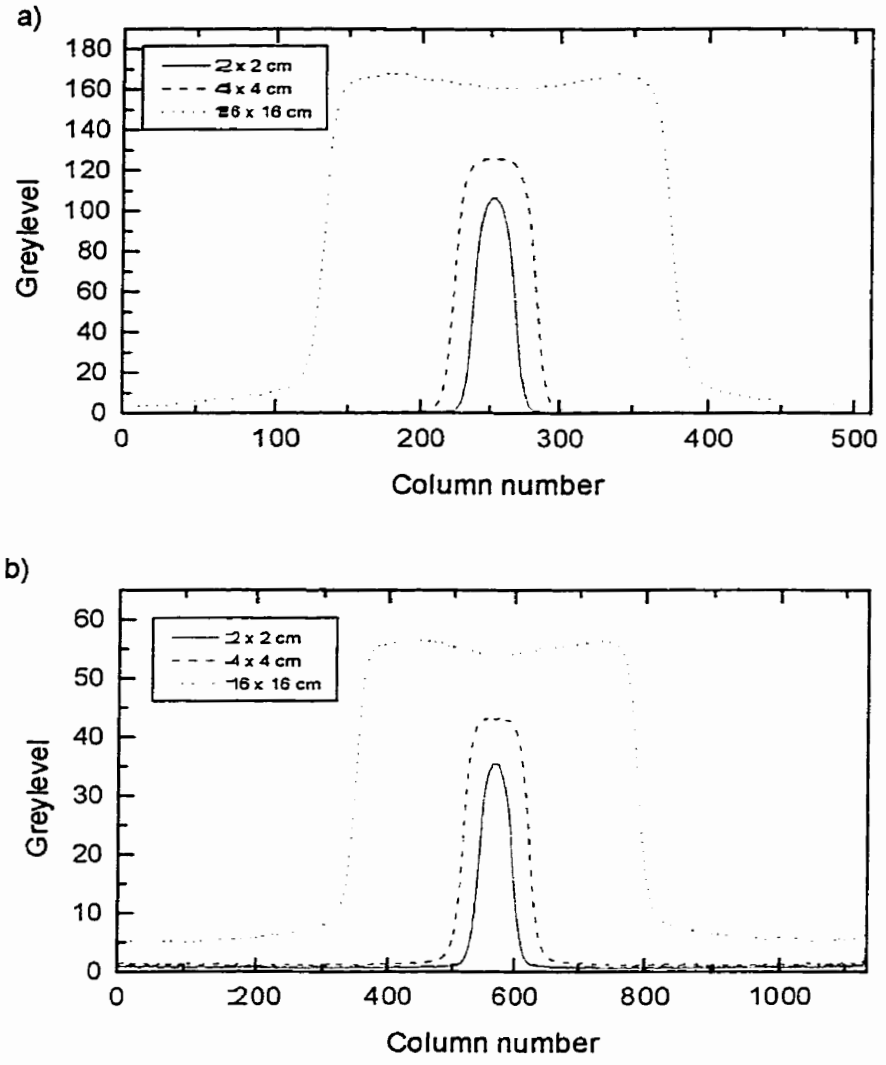

Figure 4-3 Profiles of images of radiation fields for a) the Newvicon camera, and b) the CCD camera, for square field sizes of 2 cm, 4 cm, and 16 cm at isocentre.

4.3.2 Equivalence of circular and square fields

It was possible to collect light field glare data for both circular and square fields. Since the MX2 is not equipped with a multi-leaf collimator, it was not possible to acquire radiation data for circular fields. However, the data sets with and without the mirror

(experiments B and C) were collected for both circular and square fields. The plots in Figure 3-17 and Figure 3-18 show that the response of the system was essentially the same for circular and square fields of a given area. For any given measurement, one shape appeared to result in a higher response than the other, but this trend was seen to reverse itself for subsequent measurement.

This may be explained by recalling that although the circular and square collimators were centred as well as possible in the field of view of the camera, it was not possible to centre them perfectly. In fact, a survey of the centre locations of the different data sets (see Table 9) indicates a standard deviation as large as 0.46 cm for the Newvicon camera measurements and 0.28 cm for the CCD camera measurements.

Camera	Shape	Experiment	X	Y
Newvicon	squares	A	252	230
	circles	B	245	255
	squares	B	255	244
	circles	C	262	238
	squares	C	258	240
		MEAN (pixels)	**254.4**	**241.4**
		SD (pixels)	**6.4**	**9.2**
		SD (cm)	**0.38**	**0.46**
CCD	squares	A	567	238
	circles	B	568	248
	squares	B	577	258
	circles	C	548	231
	squares	C	552	241
		MEAN (pixels)	**562.4**	**243.2**
		SD (pixels)	**12.1**	**10.3**
		SD (cm)	**0.19**	**0.28**

Table 9 Summary of location of the centres (X,Y) of the shapes used in glare measurements

For experiment B, which included the mirror, the glare measurements made closer to the top of the mirror (squares for the Newvicon camera, circles for the CCD camera) showed a higher response for larger field sizes (see Figure 3-17). For the experiments without the mirror, the circular and square field data agreed well within the noise present.

The nonuniformity in response from top to bottom of the mirror must have some effect on the difference in response between circular and square fields.

However, since this change in response seemed to depend on position of the centre rather than the shape, it was concluded that squares and circles could be treated in the same manner if the area of each was used as the descriptive parameter.

4.3.3 Causes of glare

Comparison of the glare measurements shown in Figure 3-15, Figure 3-17, and Figure 3-18 point to the mirror and light-tight box system as the source of the increase in glare for larger field sizes. For the data acquired without the mirror and light-tight box (Figure 3-18), after an initial sharp rise, the data levels off.

The plateau regions of the plots, as outlined in Table 10, were fit to straight lines to determine if there was a significant difference in slope. The parameters of these fits are shown in Table 10.

The last column of Table 10 shows the percent change in greylevel over the range $x = 95$ cm^2 to $x = 256$ cm^2. This range was selected because it was the largest range which was valid for all the fits.

There is a difference between the two cameras in the range used for fitting the data from experiment C. This is due to difficulties with that particular data set for the Newvicon camera. First, the two highest data points (beyond $x = 256$ cm^2) for the Newvicon camera were discarded, because the aperture was accidentally bumped during the measurements. This caused a sudden decrease in light level of 10% for the last two points, which was not noticed until the data were analyzed. Second, the "leveling-off" region for the Newvicon camera started at a larger field size than for the CCD camera.

From Figure 3-18 it can be seen that this is partly due to the noise present in the data. Because of this, for that fit only, the circular data was also used to increase the number of data points used in the fit.

Camera	Experiment	x-range used (cm^2)	Slope	Intercept	χ_ν^2	% change from x = 95 to x = 256
Newvicon	A	49-767	0.034 ± 0.002	136.4 ± 0.5	7.693	3.8
	B	49-400	0.026 ± 0.001	169.2 ± 0.3	0.355	2.4
	C	95-256	0.010 ± 0.004	140.1 ± 0.7	8.147	1.3
CCD	A	49-767	0.64 ± 0.04	1780 ± 10	3.032	5.3
	B	49-400	0.58 ± 0.03	3509 ± 6	0.458	2.6
	C	64-400	0.17 ± 0.05	5400 ± 10	0.169	0.5

Table 10 Parameters of fits for the linear portions of the glare data. Only square field data were used, with the exception of Newvicon, experiment C, which combined the square and circular data to provide a better fit.

Table 10 indicates that the a drastic change in glare is experienced when the mirror and light-tight box are introduced into the system. For the Newvicon camera, the glare increases nearly by a factor of 2, while for the CCD camera, the glare increases by a factor of 5. The difference between the two cameras may be due to differences in lens quality and size, as well as the slight difference in the distance of the cameras from the mirror. Another increase of a factor of 2 for both cameras is observed when the brass and the radiation are introduced into the system. Since the phosphor screen had been used for experiment B, the only difference between experiments B and A was the presence of the radiation field and the brass plate. The reflective properties of the phosphor screen would have remained the same. Therefore, the brass plate and the radiation both contribute to the glare observed on the central axis.

4.3.4 Spatial dependence of glare

To determine if the increase in EPID sensitivity near the bottom of the mirror had anything to do with the veiling glare measurements, experiment B was repeated with the squares centred at a point near the top of the screen (near the mirror) and a point near the bottom of the screen (away from the mirror). The field sizes used ranged from 4 x 4 cm^2 to 16 x 16 cm^2. The 16-cm collimator was placed so that it just lined up with the edge of the field of view for each camera, and a series of measurements were taken. These data are shown in Figure 4-4.

The data acquired near the bottom of the mirror show a higher overall greylevel. This trend is expected, since the EPID is more sensitive in the bottom region of the mirror.

However, the differences in percent change in greylevel over those ranges is not as easy to explain. A summary of the percent changes over the range plotted in Figure 4-4 ($x = 16$ cm^2 to $x = 256$ cm^2) is shown in Table 11. The percent changes over the same range when the glare measurements are made in the centre of the field of view are included in Table 11 for comparison.

The change in EPID response which occurs for light fields centred at the top and middle of the mirror is at least double that for light fields centred near the bottom of the mirror. Obviously there is something contributing to the glare in addition to the increased sensitivity. Munro [Mu98] has constructed a model which shows that light reflected back toward the phosphor could re-excite the phosphor and produce additional light photons, which would contribute the glare. The increased glare observed as the light fields get closer to the top of the mirror would appear to support that theory. This

may not be a factor for the smaller fields (3 cm x 3 cm) that were used in the sensitivity measurements, but the glare measurements used much larger field sizes. With more photons illuminating a larger part of the system, reflections within the light-tight box may become significant, and the possibility for scattered light to be detected in the ROI is increased.

Camera	Location of centre	Coordinates (pixels)	Coordinates (cm)	Percent change
Newvicon	Top	(267, 145)	(0.65, 4.73)	8 %
	Middle	(255, 244)	(-0.06, 0.20)	11 %
	Bottom	(274, 334)	(1.06, -4.68)	4 %
CCD	Top	(559, 139)	(-0.28, 6.34)	9 %
	Middle	(577, 258)	(0.35, 0.92)	8 %
	Bottom	(562, 348)	(-0.18, 6.41)	3%

Table 11 Percent change over the range x = 16 cm^2 to x = 256 cm^2 for the different light field positions.

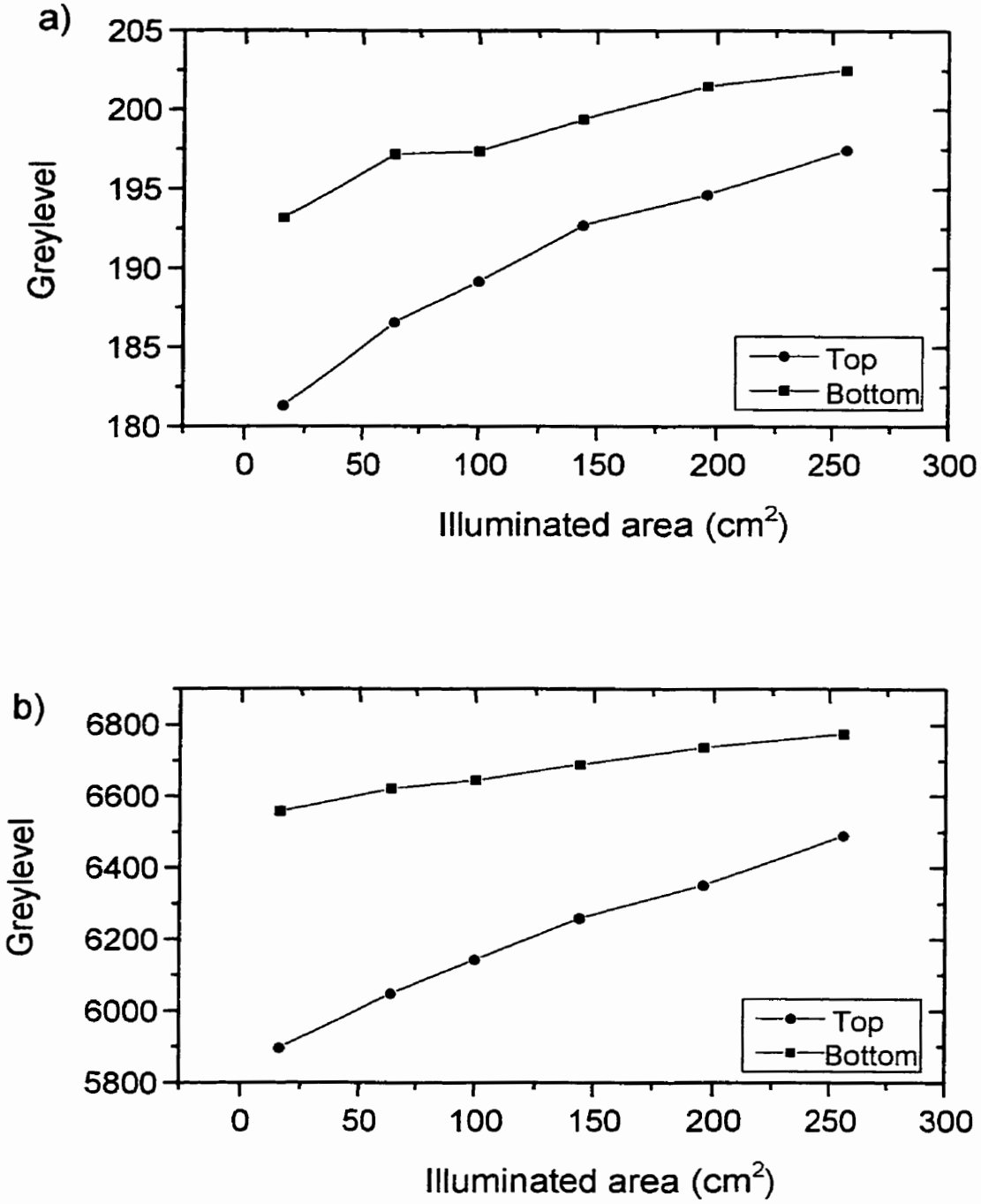

Figure 4-4 Glare measurements for square light fields centred at points near the bottom (ν) and top (λ) of the field of view for a) the Newvicon camera, and b) the CCD camera. The error bars are too small to be seen on this scale.

4.4 Dosimetry

A careful study of Figures 3-20 (a) and 3-21 (a) reveals primarily that the results from the Newvicon camera are not to be trusted, due to the problem of missing frames discussed in 4.1.2.1. The points which make the lines appear noisy are the data points where insufficient numbers of frames were acquired. By comparison, the CCD camera plots in Figures 3-20 (b) and 3-21 (b) show very "good" behaviour of the measured greylevel with change in absorber thickness.

If the EPID were an ideal detector, both plots in Figure 3-21 should be horizontal lines, and all four lines for the different field sizes should lie on top of each other. Ignoring the points which are obviously in error due to the missing frames, there is still a definite change in greylevel recorded by the EPID for different field sizes, even when the dose is corrected for. Two factors contribute to this increase: veiling glare, and spectral effects in the EPID.

The data from Figure 3-21 were analyzed as a function of field size for different phantom thicknesses, to determine if the phantom contributed to the glare. Figure 4-5 shows a plot of these data for phantom thicknesses of 23.9 cm, 11.9 cm, and 4.0 cm.

The change in greylevel with field size was then compared to the change in greylevel observed with an open field (veiling glare experiment A). For a rough estimate, the percent change between the two extremes of field size shown in Figure 4-5 was used for comparison. Table 12 shows a summary of these numbers for the CCD camera data only. (The Newvicon data will not be considered here, because of the errors in the number of frames acquired, as discussed in Section 4.1.2.1.)

From the data shown in Table 12, it would appear that only part of the effect is caused by veiling glare from the light photons. A rough calculation from the numbers shown seems to indicate that of the 24% variation observed for the largest phantom thickness (23.9 cm), 11% is due to optical veiling glare, 8% is due to the radiation field, and an additional 5% is due to the presence of the phantom itself. For the smallest phantom thickness (4.0 cm), only about 1% of the increase can be attributed to the presence of the phantom.

Phantom thickness	Percent change
23.9 cm	23.7 %
11.9 cm	22.7 %
4.0 cm	20.0 %
0 cm (radiation field)	18.9 %
0 cm (light field, extrapolated)	11.1 %

Table 12 Percent change in greylevel for the CCD camera data for different phantom thicknesses, for field sizes ranging from 48.0 cm^2 to 767.3 cm^2.

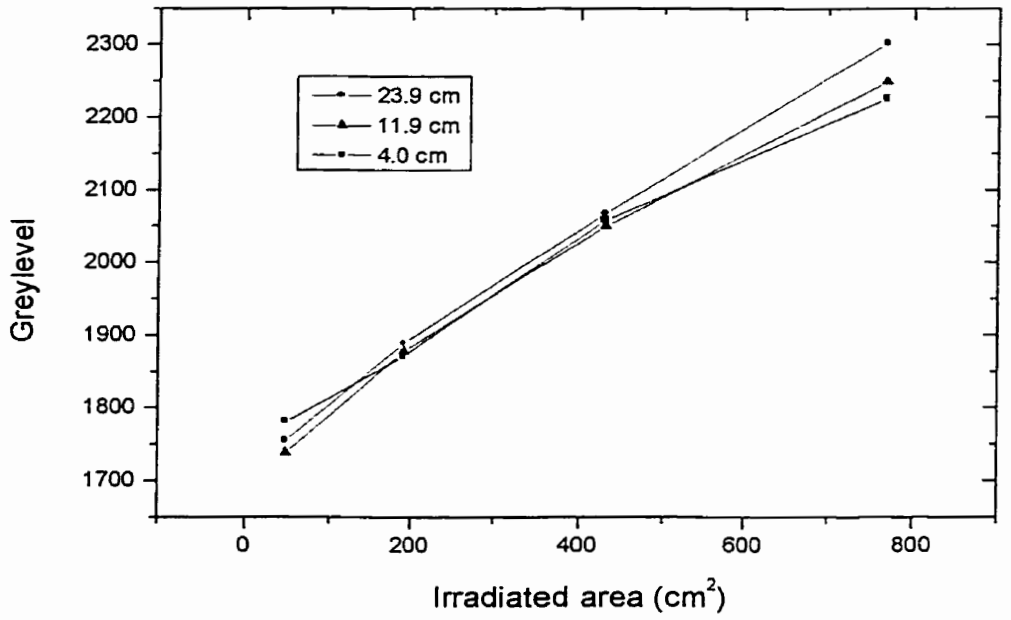

Figure 4-5 Plots of data from Figure 3-21 as a function of field size, rather than phantom thickness, for three different phantom thicknesses: 23.9 cm (λ), 11.9 cm (σ), and 4 cm (ν). Note that the error bars are comparable in size to the data points themselves.

When a phantom is introduced into the beam, two opposing effects will be observed. First, the phantom will introduce scatter into the beam, so that the dose measured on the central axis will increase. This effect will be most noticeable for the primary beam. Second, the lower-energy photons will be preferentially attenuated, so that the average energy of the beam will increase, and the central axis dose will decrease. This effect will be most noticeable for the scatter component of the beam. Therefore, depending on whether the primary or scatter component of the beam is dominant, the dose may increase or decrease with increasing phantom thickness. Table 13 shows a summary of the flatness of the response, compared to zero phantom thickness, over the range of phantom thicknesses measured.

A closer look at Figure 3-21 (b) demonstrates these effects. For the smallest field size, where the beam is mostly made up of primary photons, the EPID response decreases by 3.4% with increasing phantom thickness, over the range shown. The data in Figure 3-21 (b) were divided by the ionization chamber reading, which is proportional to the dose. Therefore, if the dose is increasing, the EPID response would be expected to decrease when divided by the ionization chamber reading.

For the two middle field sizes shown in Figure 3-21 (b), the change in response is less than 1.5% (see Table 13). This indicates that beam hardening and scatter are approximately equal and opposite in effect. For the largest field size, the response increases by 4.2%. Larger field sizes have a greater scatter component, which would be affected by beam hardening. Therefore, the dose would decrease and the EPID response would increase.

In spite of these small variations with phantom thickness, the change in EPID response is small for all the data shown Figure 3-21 (b). The dependance on phantom thickness varies from an overresponse of approximately 4% for larger field sizes to an underresponse of approximately 3% for small field sizes, with intermediate field sizes exhibiting an underresponse of approximately 1%. As explained before, the plots for different field sizes do not overlap, but most of this effect is caused by glare involving light photons inside the EPID light-tight box.

Field size at the detector surface	Percent change
6.9 cm x 6.9 cm	-3.4 %
13.8 cm x 13.8 cm	-1.2 %
20.7 cm x 20.7 cm	- 0.6 %
27.7 cm x 27.7 cm	+ 4.2 %

Table 12 Summary of percent change in EPID response over the range of phantom thicknesses t from $t = 0$ cm to $t = 23.9$ cm.

5 Conclusions

The CCD camera is undoubtedly an improvement over the Newvicon camera used in the portal imaging system. The data acquired with the CCD camera show considerably less variation than the Newvicon camera in every situation. Central axis exit dosimetry, similar to that described by Kirby [Ki93, Ki95] would be possible with the CCD camera and light-tight box setup, or even with a permanent replacement of the Newvicon camera currently in use in the BEAMVIEW^{PLUS} portal imager. However, the 0.5 s delay between frames would make the quantitative use of the camera impossible for any type of dynamic therapy. In addition, software appropriate for everyday clinical use would need to be developed before a permanent installation of the CCD camera.

The spatially nonuniform response should be investigated further to conclusively determine its cause. The difference in distance between the camera and the top or bottom of the mirror has been proposed as a cause of the nonuniform response. However, other possibilities exist for the cause of this nonuniformity. For example, there could be a physical irregularity with the mirror. It may be more reflective near the bottom than near the top. If it were rotated by 180°, and the effect reversed itself, this would be shown to be the case. However, if this were attempted, and the effect did not reverse itself, the increased sensitivity could be explained by the scatter introduced by the mirror itself, as discussed.

The nonuniform glare observed in the system would make the production of dose maps by the deconvolution of EPID images quite difficult. Such a deconvolution has been performed by Pasma [Pa98], but their calculation assumed that the glare function

was spatially invariant. For the spatially variant glare observed here, measurements of the veiling glare would have to be made at all points across the EPID surface.

The Newvicon camera and software were unreliable. The software which acquired the images occasionally stopped acquisition before the radiation was off, which caused a loss in greylevel in the image. It appeared to do this randomly. Therefore, the greylevels measured by the Newvicon camera could not be used for quantitative applications.

The Newvicon camera data were noisy. The standard error in the mean greylevel did not seem to account for the actual variation in measured greylevel. This can be confirmed by the plots of Newvicon camera data, which displayed more variation than the error bars accounted for. A systematic uncertainty which changed from frame to frame might account for such variation. It could cause the greylevel to be higher or lower for a given frame, but still result in a small standard error.

Even though the CCD camera was a clear improvement over the old Newvicon camera, the nonuniform veiling glare would make deconvolution of EPID images for portal dose maps extremely difficult. Nevertheless, this system could be calibrated to give measurements of central axis exit dose.

6 Acknowledgements

I would like to take this opportunity to thank all the staff and students of the Medical Physics Department at CancerCare Manitoba. A special thank you is in order for my electronics buddy, Brian Myslicki, a source of infinite BEAMVIEW^{PLUS} knowledge, who spent countless hours patiently working with me and the MX2 to get things working just right. Financial support was provided by the National Sciences and Engineering Research Council (NSERC) and the University of Manitoba.

7 References

[Ab95] T. M. C Abbott, "*In situ* CCD testing." (1995) [On-line] Available: http://www.cfht.hawaii.edu/~tmca/cookbook/top.html.

[Al96] V. G. M. Althof *et al.*, "Physical characteristics of a commercial electronic portal imaging device." Med. Phys. **23**, 1845-1855 (1996).

[Ba80] Norman A. Baily, "Video techniques for x-ray imaging and data extraction from roentgenographic and fluoroscopic presentations." Med. Phys. 7, 472-491 (1980).

[Ca93] Riccardo Caladrino *et al.*, "Human errors in the calculation of monitor units in clinical radiotherapy practice." Radiother. Oncol. **28**, 86-88 (1993).

[DB99a] DBS Imaging. "Camera Technical Notes." (1999) [On-line] Available: http://www.dbs-imaging.com/new_web/engli...essing/technical_notes/cameras/index.htm.

[DB99b] DBS Imaging. "Lenses." (1999) [On-line] Available: http://www.dbs-imaging.com/new_web/engli.../technical_notes/lenses/lenses_intro.htm.

[Di95] M. L. P. Dirkx *et al.*, "Daily dosimetric quality control of the MM50 Racetrack Microtron using an electronic portal imaging device." Radiother. Oncol. **37**, 55-60 (1995).

[Fi98] H. Fielding, "An Investigation of the BEAMVIEW^{PLUS} Portal Imager for Dosimetry Measurements". Unpublished manuscript, University of Manitoba, 1998.

[Ha93] E. J. Hall, Radiobiology for the Radiologist. (J. B. Lippincott Company, Philadelphia, 1993).

[Hec74] E. Hecht and A. Zajac, Optics. (Addison-Wesley Publishing Company, Reading, 1974).

[Hei95] B. J. M. Heijmen *et al.*, "Portal dose measurement in radiotherapy using an electronic portal imaging device." Phys. Med. Biol. **40**, 1943-1955 (1995).

[IC76] International Commission on Radiation Units and Measurements (ICRU), *Determination of Absorbed Dose in a Patient Irradiated by Beams of X or Gamma Rays in Radiotherapy Procedures*, Report 24 (1976).

[IC93] International Commission on Radiation Units and Measurements (ICRU), *Prescribing, Recording, and Reporting Photon Beam Therapy*, Report 50 (1993).

[Ke81] *Kempe's Engineers Year-Book*, Vol. 1, edited by John P. Quayle (Morgan-Grampian Book Publishing Co. Ltd., London, 1981) p. A1/18.

[Ki93] M. C. Kirby and P. C. Williams, "Measurement possibilities using an electronic portal imaging device." Radiother. Oncol. **29**, 237-243 (1993).

[Ki95] M. C. Kirby and P. C. Williams, "The use of an electronic portal imaging device for exit dosimetry and quality control measurements." Int. J. Radiation Oncology Biol. Phys. **31**, 593-603 (1995).

[Le92a] G. Leunens *et al.*, "Human errors in data transfer during the preparation and delivery of radiation treatment affecting the final result: 'garbage in, garbage out'." Radiother. Oncol. **23**, 217-222 (1992).

[Le92b] G. Leunens *et al.*, "Assessment of dose inhomogeneity at target level by in vivo dosimetry: can the recommended 5% accuracy in the dose delivered to the target volume be fulfilled in daily practice?" Radiother. Oncol. **25**, 242-250 (1992).

[Ma81] S. Martin, "Survey of glare measurements in optical instruments." in *Proc. SPIE 274: Assessment of Imaging Systems: Visible and Infrared*, edited by T. L. Williams (The International Socity of Optical Engineering, Bellingham, 1981) pp. 288-308.

[Mi91] C. Mitine *et al.*, "Is it necessary to repeat quality control procedures for head and neck patients?" Radiother. Oncol. **21**, 210-210 (1991).

[Mu95] P. Munro, "Portal Imaging Technology: Past, Present, and Future." Seminars in Radiation Oncology **5**(2), 115-133 (1995).

[Mu98] P. Munro et al., "Glaring errors in transit dosimetry." *EPI 98: 5th International Workshop on Electronic Portal Imaging: Program and Abstract Book.* (Phoenix, 1998).

[NA99] North American Imaging. "Camera Tube Descriptions." (1999) [On-line] Available: http//www.tubenet.com/camera.html.

[NC00] National Cancer Institute of Canada: Canadian Cancer Statistics 2000, Toronto (2000).

[No95] A. Noel *et al.*, "Detection of errors in individual patients in radiotherapy by systematic in vivo dosimetry." Radiother. Oncol. **34**, 144-151 (1995).

[Pa98] K. L. Pasma *et al.*, "Accurate portal dose measurement with a fluoroscopic electronic portal imaging device (EPID) for open and wedged beams and dynamic multileaf collimation." Phys. Med. Biol. **43**, 2047-2060 (1998).

[Po99] Polaris Industries. "C-Mount vs. CS Mount" (1999) [On-line] Available: http://www.polarisusa.com/C-Mount.htm.

[Rad93] T. Radcliffe *et al.*, "Monte Carlo optimization of metal/phosphor screens at megavoltage energies." Med. Phys. **20,** 1161-1169 (1993).

[Raj95] P. R. D. Rajapakshe, "Optimization of a real-time portal imaging system for quantitative imaging." PhD thesis, University of Manitoba (1995).

[Sh95] S. Shalev, "Treatment Verification using digital imaging." in *Medical Radiology: Radiation Therapy Physics*, edited by A. R. Smith (Springer-Verlag, New York, 1995) pp. 155-173.

[Sh96] S. Shalev, "Megavoltage Portal Imaging." In *Teletherapy: Present and Future. Proceedings of the 1996 Summer School*, edited by J. Palta and T. R. Mackie (Advanced Medical Publishing, Madison, 1996) pp. 445-469.

[TI96] Texas Instruments, *Production data sheet: TC217, 1158 x 488-pixel CCD image sensor*. (Texas Instrucments Incorporated, Dallas, 1996). [On-line] Available: http://www-s.ti.com/sc/psheets/socs015c/socs015c.pdf.

[Vi90] A. G. Visser *et al.*, "Performance of a prototype fluoroscopic radiotherapy imaging system." Int. J. Radiation Oncolcogy Biol. Phys. **18**, 43-50 (1990).

[Wo94] B. Wowk *et al.*, "Optimization of metal/phosphor screens for on-line portal imaging." Med. Phys. **21**, 227-235 (1994).